RSC Advances

REVIEW

View Article Online
View Journal | View Issue

Cite this: *RSC Adv.*, 2024, **14**, 11411

Role of transition metals in coinage metal nanoclusters for the remediation of toxic dyes in aqueous systems

Priyanka Sharma, Mainak Ganguly * and Mamta Sahu

A difficult issue in chemistry and materials science is to create metal compounds with well-defined components. Metal nanoclusters, particularly those of coinage groups (Cu, Ag, and Au), have received considerable research interest in recent years owing to the availability of atomic-level precision *via* joint experimental and theoretical methods, thus revealing the mechanisms in diverse nano-catalysts and functional materials. The textile sector significantly contributes to wastewater containing pollutants such as dyes and chemical substances. Textile and fabric manufacturing account for about 7×10^5 tons of wastewater annually. Approximately one thousand tons of dyes used in textile processing and finishing has been recorded as being discharged into natural streams and water bodies. Owing to the widespread environmental concerns, research has been conducted to develop absorbents that are capable of removing contaminants and heavy metals from water bodies using low-cost technology. Considering this idea, we reviewed coinage metal nanoclusters for azo and cationic dye degradation. Fluorometric and colorimetric techniques are used for dye degradation using coinage metal nanoclusters. Few reports are available on dye degradation using silver nanoclusters; and some of them are discussed in detailed herein to demonstrate the synergistic effect of gold and silver in dye degradation. Mostly, the Rhodamine B dye is degraded using coinage metals. Silver nanoclusters take less time for degradation than gold and copper nanoclusters. Mostly, H_2O_2 is used for degradation in gold nanoclusters. Still, all coinage metal nanoclusters have been used for the degradation due to suitable HOMO–LUMO gap, and the adsorption of a dye onto the surface of the catalyst results in the exchange of electrons and holes, which leads to the oxidation and reduction of the adsorbed dye molecule. Compared to other coinage metal nanoclusters, Ag/g-C_3N_4 nanoclusters displayed an excellent degradation rate constant with the dye Rhodamine B (0.0332 min^{-1}). The behavior of doping transition metals in coinage metal nanoclusters is also reviewed herein. In addition, we discuss the mechanistic grounds for degradation, the fate of metal nanoclusters, anti-bacterial activity of nanoclusters, toxicity of dyes, and sensing of dyes.

Received 5th February 2024
Accepted 26th March 2024

DOI: 10.1039/d4ra00931b

rsc.li/rsc-advances

Department of Chemistry, Manipal University Jaipur, Dehmi Kalan, Jaipur 303007, India. E-mail: humansense2009@gmail.com

Priyanka Sharma

Priyanka Sharma obtained her BSc and MSc degrees from Maharaja Brij University in India. She is now pursuing her PhD from Manipal University Jaipur, India, under the guidance of Dr Mainak Ganguly. Her area of interest is materials science and environmental science.

Mainak Ganguly

Dr Mainak Ganguly received his PhD from Indian Institute of Technology, Kharagpur, India, in 2014. He had acted as post-doctoral researcher up to 2019 in Furman University (USA) and McGill University (Canada). He is currently working as an Asst. Professor in the Department of Chemistry, Manipal University Jaipur (India). His research interests include nanoparticles, clusters, biophysical chemistry, environmental remediation, etc. He has published more than 55 papers and two book chapters.

1. Motivation

The widespread presence of organic dyes in industrial wastewater from the paper, textile, and garment industries pollutes the environment significantly.[1] According to multiple investigations, 10–12% of dyes used in the textile industry are lost during synthesis and processing activities and end up in wastewater.[2–6] These dye-polluted effluents contain colors that are non-biodegradable, extremely toxic, and detrimental to living organisms.[7,8] Dyes are vividly visible in water even at extremely low concentrations (<1 ppm) and can damage aquatic habitats.[9–11] As a result, color removal from wastewaters is critical.[12] Contamination by different dyes poses serious threats to mankind. A handful of review articles have been published on sensing using coinage metal nanoparticles and nanoclusters. Kanelidis *et al.*[13] reviewed the role of ligands in coinage metal nanoparticles for electronics. Chinta *et al.*[14] summarized colorimetric tests for natural amino acids using coinage metal nanoparticles. Sharma *et al.*[15] reviewed coinage metal-enhanced fluorescence using diiminic Schiff bases for the selective and sensitive detection of aqueous pollutants. Similarly, metal nanocluster-based luminescent biosensors *via* etching chemistry were reviewed by Si *et al.*[16]

Nanostructures are classified into nanoparticles (PNls) and nanoclusters (CNs) depending on their size. Size alteration is also related to various physico-chemical properties. CNs exhibit fluorescence due to d–d transition. Moreover, their ultra-small size is related to a very high surface area. Dye degradation with nanoparticles has already been reviewed. Metal nanoclusters of Cu, Ag, and Au for dye degradation is a very important area for environmental remediation and needs to be reviewed in detail. In the present manuscript, a comparative study of coinage metal nanoclusters for dye degradation was reviewed along with dye sensing. This review article may be an important for young researchers to venture into the field of sensing based on dye degradation.

2. Introduction

Significant efforts have been undertaken in recent years to investigate the photophysical and photochemical behavior of multicomponent nanostructured assemblies made up of metals, semiconductors, and photoactive dyes.[17–29] Metal nanoclusters (CNsM) are molecularly precise structures made up of a certain number of metal atoms plus capping ligands. Their emergence bridges the gap between tiny molecules and nanomaterials, allowing for a better grasp of many fundamental elements of science.[30] CNsM's physical and chemical characteristics are heavily influenced by their core structure as well as the arrangement of their surface ligands. Atomically defined gold, silver and copper CNs are a special type of CNsM that are used in catalysis, optics, biology, and sensing.[31–34] Coinage CNsM with atomically precise structures, such as Au, Ag, and Cu, can be regarded as extreme-trivial metal nanoparticles (PNlsM), aggregated from dozens to hundreds of metal atoms protected by single-layer organic ligands. They are metal atom aggregates with sizes generally less than 3 nm, occupying the transition scale among metal-atom and plasmonic PNlsM.[35–37] Because CNsM is much smaller than PNslM, the initial surface plasmon resonance effect vanishes. As the particle size is close to the Fermi wavelength, significant alterations take place in the particle's energy levels. This is the result of the quantum size effect, which causes the electron levels of CNsM the transition from a quasi-continuous to a discrete state. This leads to molecular-like behaviors (intense fluorescence due to energy gaps between the LUMO and HOMO).[38]

Due to the presence of electrons with incomplete d-orbitals in their atomic structures, transition metals are categorized as d-block elements.[39] They differ from the core group elements in both their physical and chemical properties. Because the energy levels of the d and ns shells are so close together, these elements may show a variety of oxidation states, making them relevant for further study. The range of applications for transition metals is widened as a result as there are an enormous number of oxide combinations possible.[40,41]

Because of its stability, nontoxicity, and high electronegativity, gold (Au) is the most appealing choice for noble metal-based photocatalysts.[42] Fluorescent gold CNs (CNsAu), aggregation of numerous to tens of metal-atoms, have piqued the interest of scientists in recent years due to their exceptional optical, electro-magnetic, and catalytic properties resulting from their very tiny size (2 nm).[43–46] Few-atom CNsAu are difficult to fabricate due to their strong aggregation tendency. However, several synthetic approaches have been successfully developed to produce CNsAu with unique properties, showing great and broad applicability in diverse fields like bio-imaging, chemo-sensing, and catalysis.[47–51] The formation of CNsAu and CNsAg has also received a lot of attention in investigations on noble metal CNs. In comparison to other precious metals, copper is comparatively plentiful and cheap.[52–57] CNsCu, on the other hand, are less stable because of their high oxidation susceptibility, and their fluorescence quantum yield (QY) is lower.[58] In recent years, efforts have been undertaken to enhance the physicochemical and optical characteristics of CNsCu to widen their usefulness in a variety of domains, including sensing and nanodrugs.[59] Because of their strong photo-stability, high QY emitters, and less toxicity, ligand-protected CNsAg have attracted a lot of interest as new

Mamta Sahu

Mamta Sahu received her BSc from Subodh Girls PG collage (Jaipur, India) and MSc degree from RK PG collage (Jaipur, India). She is currently pursuing her PhD under the supervision of Dr Mainak Ganguly from Manipal University Jaipur, India. Her area of interest is environmental nanoscience.

fluorophores. These characteristics render them suitable for use in microscopy settings when DNA is used as a template, with potential biocompatibility and applications in bio-labeling and sensing.

In this review article, we concentrated on the coinage metal CNs for the elimination of hazardous dye both *via* adsorption and degradation with plausible mechanisms. Moreover, the role of transition metals in such removal processes was also reviewed. The sensing of the dye is discussed here with coinage metal clusters.

3. Dye

Unlike pigments, which chemically bind to the substrate they color, dyes are colored substances that link chemically to the surface (they are applied to). To make dye faster on fiber, a mordant may need to be added. Dye is frequently applied in an aqueous solution.[60] Textile dyes, like a wide range of industrial contaminants, are exceedingly poisonous and potentially carcinogenic and have been connected to several diseases in people and animals as well as environmental damage.[61] Colors in sediments and soil bioaccumulate are transferred to public water supply systems using their refractory nature under aerobic circumstances, especially in conventional treatment facilities. As the reduction of azo-type compounds leads to risky aromatic amines, they can be partially destroyed or transformed in the presence of anoxic sediments despite the majority's resilience to the environment. Another potential is that dyes will be combined with intermediate synthetic chemicals or their breakdown products to produce new mutagenic and carcinogenic substances. Dyes have many applications and can be found in the effluents of numerous manufacturing and processing units; hence, their discharge has a significant environmental effect. As waste from several industries produces significant pollution, protecting the environment becomes a difficult task. The economy of Asia and other nations is significantly influenced by the textile sector. The textile industry often uses dyes to color fabrics.[62] A very little amount of dye in the water is extremely noticeable and can be hazardous to aquatic life. In the textile company, substantial volumes of aqueous wastes and dye effluents with strong persistent color and high biological oxygen demand (BOD) loading are released from the dyeing process, which are both aesthetically and ecologically unsatisfactory.[63] Dyes are organic compounds with a complex aromatic molecular structure that may give other things a brilliant and vivid color. However, dyes' complex aromatic molecular structures make them exceedingly durable, making biodegradation more challenging.[64] Dyes are generally found in dye house effluent at concentrations ranging from 10 to 50 mg L^{-1}; nevertheless, color has been observed at concentrations greater than 1 mg L^{-1}. Except for the dye, most contaminants may be eliminated using chemical and physical processes. Metals are sequestered by synthetic dyes, producing microtoxicity in fish and other aquatic creatures.[65–67]

Fig. 1 displays the toxicity of dyes in wastewater, the treatment of the dye-contaminated wastewater, and the dye degradation mechanism in a schematic form.

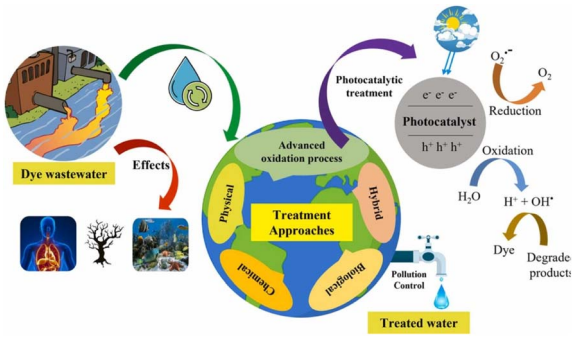

Fig. 1 Toxicity of dyes in wastewater. Reproduced with permission from ref. 67, copyright 2024, *J. Environ. Chem. Eng.*

3.1 Classification of dyes

Dyes can be classified into two classes based on their chemical structure and application techniques [Fig. 2]. However, dyes such as methylene blue, Rhodamine B, methyl orange, congo red, amido black 10b, and coumarin are utilized extensively in textile and natural life. These colors are also poisonous and detrimental to human health. These dyes are so far reported to be degraded using coinage CNsM.

3.1.1 Congo red. Humanity faces a grave peril as clean water resources deteriorate over time. When industrial effluent is released into bodies of water, it pollutes the water. The textile industry is one of the largest suppliers of worldwide water contamination, and each year, about 80×10^{-4} tons of azo dyes (AD) are generated globally. Although about 80% of AD is used in textiles for material coloring, 10–15% is lost through wastewater. By altering the pH and inorganic chemical composition of water, AD raises the chemical and biological oxygen requirement. Congo red is one of the most prevalent colors used

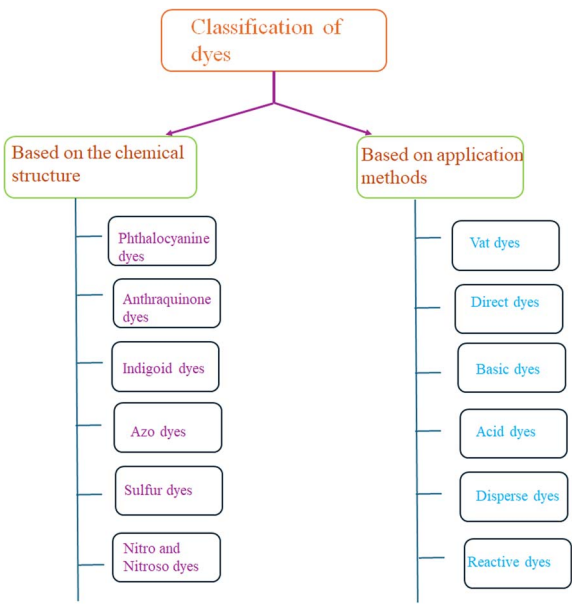

Fig. 2 Classification of dye based on chemical structure and applications.

in the textile industry. It is an anionic di-AD based on benzidine. Because this dye is known to be converted into benzidine, a human carcinogen and mutagen, it is prohibited in several countries.[68]

3.1.2 Methylene blue. Dyes are a type of organic chemical that is widely used in the textile, printing, and food industries. Dye runoffs have a significant detrimental impact on the environment, with most of them being highly poisonous and non-biodegradable.[69,70] Methylene blue (MB) is a very poisonous and carcinogenic phenothiazine derivative used in textile dyeing.[71] Methylene blue (MB) is utilized in a variety of sectors including chemical, biological, medical, and is moribund. Many side effects of MB usage include vomiting, nausea, anemia, and elevated blood pressure.[72]

3.1.3 Methyl orange (MO). MO is often used in the textile, food, paper, and leather industries. However, due to its higher toxicity, MO discharge into the environment can cause significant water pollution, and it must thus be removed from water.[73] Even a trace quantity of pigment in freshwater is unpleasant and can harm human health. Methyl orange is an anionic molecule that becomes an AD due to the inclusion of an N_2 component in its structure, which can induce allergies and hypersensitivity.[74] In humans, a high concentration of this dye can cause significant corneal harm if it comes into contact with the eye. Its low concentration in drinking water causes headaches, anemia, stomach discomfort, nausea, dizziness, mental disorientation, and excessive perspiration. As a result, its presence may result in major health issues.[75–77]

3.1.4 Malachite green (MG). MG is a triphenyl methane dye that has been extensively utilized in the manufacture of ceramics, leather, textiles, food coloring, cell coloring, and other products. Because of its great disinfection efficacy, it has also been employed in the aquaculture sector to cure scratches on fish bodies and protect against bacterial infections. However, during the 1990s, researchers have shown that MG and its reduced variants are very poisonous, persistent, carcinogenic, and mutagenic. If spilled into a body of water, it will cause irreversible environmental harm.[78,79]

3.1.5 Rhodamine B. Rhodamine B (Rh-B) is a well-known fluorescent water tracer that is frequently utilized as a colorant in textiles and food products.[80] It is toxic to both humans and animals and causes skin, eye, and respiratory system irritation. Human and animal carcinogenicity, reproductive and developmental toxicity, neurotoxicity, and chronic toxicity are caused by Rh-B dye.[81] Rh-B, one of the most extensively used organic dyes, has been recognized as a carcinogen by the International Agency for Research on Cancer (IARC). Rh-B is a pigment that is extensively used in textiles, paper, printing, and food products. Because of its toxicity profile, its discharge into the environment as wastewater poses major health risks.[82–85] It causes carcinogenesis and neurotoxicity. Specific issues include nausea, vomiting, respiratory issues, and gastritis. RhB is tough to break down [Fig. 3].[86]

3.1.6 Amido black 10B. Amido black 10B (AB-10B) is an acidic synthetic dye with two azo groups and is extensively used for coloring textile items. AB-10B, a protein-containing

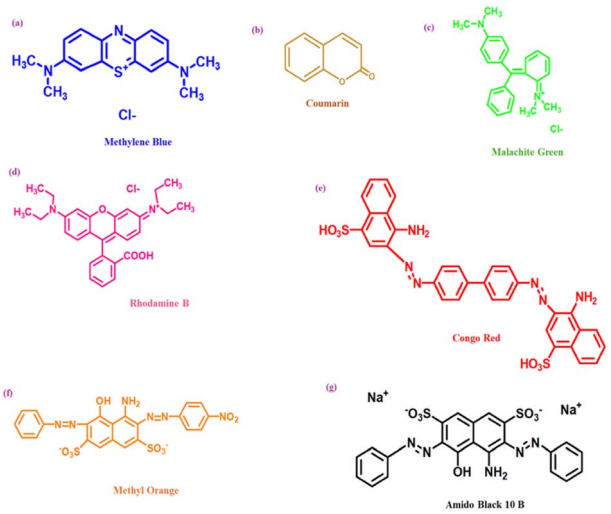

Fig. 3 Structure of different dyes [(a) methylene blue, (b) coumarin, (c) malachite green, (d) rhodamine B, (e) congo red, (f) methyl orange and (g) amido black 10B] degradable *via* CNsM.

stain, is very hazardous to humans. AB-10B is a dye that is resistant to decolorization and has minimal bio-degradation in aqueous solutions. It is often used to remove dyes from printing and dyeing effluent using various treatment methods.[87]

3.1.7 Coumarin dye. Coumarin is mildly toxic to rodent livers and kidneys, with a median fatal dosage (LD_{50}) of 293 mg kg^{-1} in rats, which is modest in comparison to other chemicals. Coumarin is harmful to the liver in rats but less so in mice.[88] It is primarily metabolized by rodents to 3,4-coumarin epoxide, a poisonous, unstable molecule that, with further differential metabolism, may induce liver cancer in rats and lung cancers in mice.[89]

4. Nanocluster

Specific formulas can describe nanoclusters, much like well-characterized organic or organometallic materials. These CNs-based molecules represent inorganic–organic hybrid substances that act as a crucial link in communicating between atoms and PNls. Their ultrasmall size, ranging from sub-nanometer to two/three nanometers in size for the metal core,[90–93] positions them as a "missing link." These CNs exhibit robust quantum size effects (characterized by distinct electronic energy levels), numerous absorption bands resulting from one-electron transitions, enhanced emission, magnetic behavior, remarkable catalytic reactivity, and nonlinear optical characteristics.[94–96] A scale function of atomicity within the cluster, derived from the energy variations between the HOMO & LUMO, indicates that CNsM with dimensions akin to the electron's Fermi wavelength (approximately 0.7 nm) and size-dependent fluorescence displays molecule-like characteristics with quantifiable electronic properties and luminescence.[97–100] Because of the quantum size effect, the size of the CNs is critical for their catalytic activity. Furthermore, the unsaturated

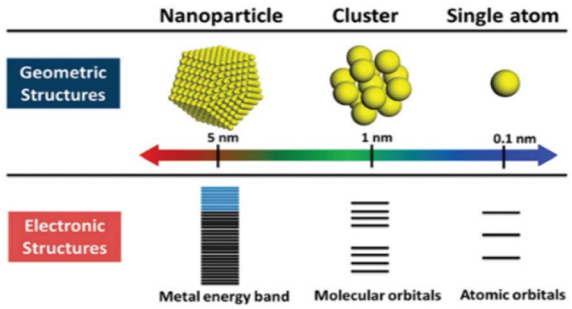

Fig. 4 Comparison between geometric and electronic structures of the nanoparticle, cluster, and single atom. Reproduced with permission from ref. 100, copyright 2024, *Nanoscale*.

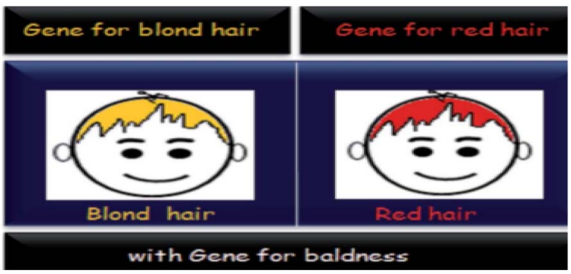

Fig. 5 Baldness genes were epistatic to blond or red hair genes. Reproduced with permission from ref. 103, copyright 2024, and *RSC Advances*.

coordination site with increased d-band energy improves the catalytic reactivity [Fig. 4].

5. Synergistic effect

The synergistic effect refers to the combined influence of more than one species when the total of their impacts exceeds the total of their combined effects.[101,102] This phenomenon is akin to epistasis, where the function of one gene is dependent on more than one modifier gene in the genetic contextual. In the context of catalysis, synergism plays a crucial role. Certain metals, including silver, copper, nickel, palladium, and cobalt, exert a significant influence on oxygen activation in gold-catalyzed oxidation processes. Notably, Ag and Au, despite being in the same group (11) in the periodic table, commonly exhibit synergistic effects. This highlights the unique interactions and enhanced catalytic outcomes that can arise from the combination of specific metal elements.[103] Au–Ag synergism in fluorescence is a very promising phenomenon, and many researchers have lately entered this area. Silver and gold bimetallic clusters have been shown to be a viable approach to circumvent the normally poor λ_{em} (in comparison to other popular fluorophores) of CNsAu since the bimetallic CNs display considerably higher QY.[104,105]

Doping is the deliberate insertion of contaminants into a pure material to modify its qualities. Doping commonly converts semiconductors to conductors, resulting in a substantial shift in band-gap energy. Significant changes are witnessed for coinage CNsM with transition metal doping owing to the shift in band-gap energy.[106,107] Doping is one kind of synergism of the d-block metal (mostly) with coinage CNsM to increase the CNs's sensitivity and surface volume [Fig. 5].[108] It has been observed that coinage CNsM cannot degrade dyes. However, doping with transition metals coinage CNsM can degrade dyes.

6. Degradation

In recent years, the elimination of dyes and other contaminants from the aquatic atmosphere has become a critical need.[109] To address it, several techniques have been developed, such as ozonation,[110] membrane filtration,[111] bioadsorption,[112,113] ion exchange removal,[114–116] adsorption,[117–120] photocatalytic degradation,[121,122] catalytic reduction,[123,124] biological/aerobic therapy,[125] and coagulation.[126] The absorption technique is often employed in prerelease removal operations because of its simplicity and low cost.[127] However, limitations such as low absorption efficacy, incomplete pollutant removal, and poor mechanical stability of adsorbents make efficient pollutant removal challenging.[128–130] Over the past several years, the photodegradation of contaminants has gained more attention. Through the process of photocatalysis, a semiconductor photocatalyst uses sunlight absorption to break down a variety of environmental pollutants, including organic pollutants in the air and water.[131–134] Photodegradation has benefits over conventional wastewater treatment processes. Numerous operational factors, such as the starting [dye], pH of the solution, exposure intensity, and temperature of the reaction, impact the whole photodegradation method from dye molecule adsorption on the photocatalyst to dye molecule destruction by reactive radicals.[135–140] For *e.g.*, Xie *et al.*[87] demonstrated that the decolorization of amino 10 B dye followed pseudo-first-order kinetics, where raising the initial dye concentration reduces the photodegradation efficiency [Fig. 6].

Table 1 demonstrated the formation of various coinage CNsM/transition metal hybrid particles. Such hybrids were utilized for dye degradation in the following sections.

6.1 CNsAu for dye degradation

6.1.1 Methylene blue. The aq. solutions of chloroauric acid and glutathione were combined, followed by the addition of Milli-Q water under stirring at 25 °C. Then, a basic solution was added in it to adjust the pH to approximately 7. The solution was left to age for about 1 h, during which the oligomeric gold(I)–thiolate complexes formed to develop the self-assembled CNs superstructures for modulating the photophysical & chemical activities of water-borne luminous CNsAu.[141] The controlled addition of tin(II) ions into individual particles led to the formation of 3D spherical tin-doped CNsAu colloidal frameworks (CNsAuF). The stability of CNsAuF(0) was influenced by the quantity of Sn^{2+}, with the zeta potential progressively increasing from +12.4 mV for CNsAu at pH 7 to a maximum of +54.9 mV, indicating outstanding colloidal stability. CNsAuF exhibited significant photocatalytic activity,

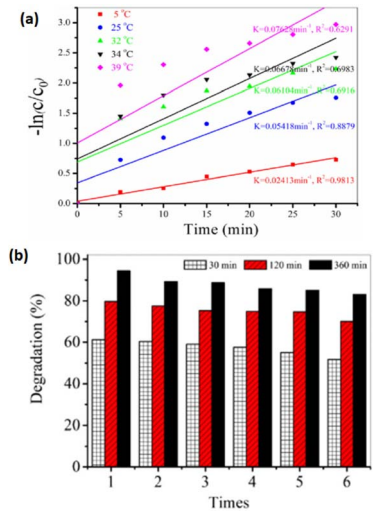

Fig. 6 Dye degradation. (a) pseudo first order; (b) reusability of dye. Reproduced with permission from ref. 87, copyright 2024, *Water Air Soil Pollut*.

enabling the elimination of MB under both UV & visible light. Specifically, under UV irradiation at a wavelength of 350 nm in the presence of tin-doped CNsAuF, a complete breakdown of MB occurred in just 5.5 min, compared to 112 min for CNsAu and over 140 min without any catalyst. The substantial enhancement in the photocatalytic activities of CNsAuF (20–25-fold) was attributed to their 3D architecture, which facilitated improved dye adsorption on both the surfaces and interiors. This unique structure contributed to the exclusive catalytic activities of CNsAuF in water[142,143] compared to individual CNsAu (+1). Importantly, CNsAuF outperformed CNsAu in terms of photoactivity induced by visible light,[144] completing the degradation in a significantly shorter time. In contrast, CNsAu required several days, and without a catalyst, the total breakdown of MB took an extended period. The researchers also noted that the catalytic activities of CNsAu and CNsAuF were low or had little effect in the absence of light or with the subsequent addition of Sn^{2+} ions into the reaction mixture without CNsAu/CNsAuF under UV light. The enhanced photocatalytic performance of CNsAuF and their potential applications in water treatment processes were reported. CNsAuF could be employed for bioimaging due to their outstanding colloidal stability and strong photoluminescence in aqueous media. They showed cell counting kit 8 (CCK-8) assays and trypan blue tests on two distinct cell lines (NIH3T3 and A549 cells) to determine the cytotoxicity of CNsAu and CNsAuF.[145–147]

The $HAuCl_4$/THF solution was combined with 10 μL of trimethoxysilane (MPTS) and subjected to UV light irradiation at 365 nm for 8 h. Over this period, the solution's color gradually transformed from nearly colorless to a pale yellow following the mixture of the two reagents. Eventually, CNsAu sol was produced. A photoreduction approach was followed to generate luminescent silane-stabilized CNsAu. The λ_{em} of the resulting CNsAu could be manipulated from 538 nm to 580 nm by varying the mole ratio of the stabilizer to the gold precursor. In the absence of light, the MB solution with CNsAu showed no discernible change, indicating the reaction was light-driven. Under continuous visible irradiation for 60 min, the [MB] only marginally reduced by 4% in the absence of CNsAu. This slight decrease could be attributed to the self-photo-bleaching action of MB, when exposed to high energy density irradiation. However, in the existence of CNsAu, the absorption of dye was significantly reduced by 95.6%, demonstrating a strong promoting impact of CNsAu on the photocatalytic degradation of MB. The intensity of the specific charge peak at 284 nm, attributed to [MB + H^+], was notably elevated, but after an hour of light irradiation, the intensity dropped dramatically and nearly vanished. No discernible intensity rise was observed for peaks at about 286 nm, 304 nm, & 308 nm, which were attributed to [MBL + H^+], [MBL + NH_4^+], & [MBL + Na^+], respectively, indicating the absence of MBL (a photoproduct of MB). The photocatalytic efficacy of CNsAu placed on substrates (CNsAu@glass) was more advantageous for catalyst recycling

Table 1 Coinage CNM-transition metal hybrid particles with different capping agents with various properties

CNs	Capping	UV (nm)	$\lambda_{em}/\lambda_{ex}$ (nm)	Hybrid	UV (nm)	$\lambda_{em}/\lambda_{ex}$ (nm)	Size (nm)	Oxidation number
Ag	Perylenetetracarboxylic acid	530	—	Ag–TiO_2/Nb_2O_5	470	—	∼2–3	0
	Histidine	254	465/373	Ag:Al_2O_3:TiO_2	—	—	∼1.6	0
	Mercaptosuccinic acid	390	—	AgQCs-GCN	—	400/350	>500	—
	Perylenetetracarboxylic acid	254	—	ZnO–Ag	—	—	1.5–2	1
	3-Aminopropyl-trimethoxysilane	∼370	380/325	ZnO@Ag	373	380/325	2.5	0
	Glutathione & $NaBH_4$	530	—	Ag–TiO_2 hybrid	454	—	<3	0
	Hydrazine hydrate	—	—	Ag/CN-sr	400	425/316	10	1
	$C_4H_6O_6$	250	—	Ag/CeO_2	320	—	5–7	0
	BSA & $NaBH_4$	305	670/420	Ag@AuCNs/f-MoS_2	305	705/420	2–3	0
	GSH	—	—	Ag–TiO_2	—	—	—	—
Cu	L-Cysteine	—	480/400	CuCNs/C–H_2O_2	—	480/400	—	0
	$C_2H_2O_4$	—	—	$(NH_4)_2CuMo_8O_{26}(C_{10}H_8N_2)_2$	—	—	—	0
	Glutathione	330	450/373	CuCNS	330	370/330	1.7	0
	Alcoholic solution	370	—	CuNa–$K_2Ti_6O_{13}$	370	—	5	2
Au	Bovine serum albumin & NaOH	—	440/375	C-dot-C153-AuCNs	—	440/375	2 ± 1	0
	GSH	395	—	GNCF-300	350	—	1	0 & 1
	5,5-Dimethyl-1-pyrroline-*N*-oxide	500	—	Au CNs@glass	655	—	∼1.3	0

compared to standalone CNsAu. Interestingly, the catalytic activity of standalone CNsAu was greater than that of CNsAu attached to glass substrates [Fig. 7]. This study highlights the potential of these CNsAu as efficient photocatalysts for the degradation of MB and suggests their applicability in catalyst recycling processes.[148] The LUMO boundary orbital of CNsAu is approximately 0.17 V concerning the SHE. The fluorescence emission energy (2.2 eV) indicates that the highly occupied molecular orbital frontier orbit was positioned at 2.3 V against SHE, significantly below the redox potential of MB/LMB (−0.4 V). According to the absorption edge of CNsAu (2.9 eV) and the position of the HOMO frontier orbital (0.17 V), an empty level at −0.50 V ought to produce photo-excited electrons.[149,150]

6.1.2 Coumarin (C153) dye. A bovine serum albumin solution was added to $HAuCl_4$ at 38 °C under vigorous stirring. Sodium hydroxide was introduced to elevate the pH of the solution. The stirring continued vigorously until the solution's color developed into a deep brown shade, typically taking about 12 h. Following this, the resulting red-emissive solution of protein-protected CNsAu underwent dialysis, with the water change performed at 2 h intervals. A composite of CDs and dye-encapsulated bovine serum albumin@protein-capped CNsAu had been produced for effective light-harvesting and white light production. CDs served as donors, whereas CNsAu capped with bovine serum albumin protein served as acceptors. C153 was insoluble in water as it entered the hydrophobic pocket of BSA. The anisotropic reorientation time $r(t)$ of C153 in ethanol solution was 120 ps. Because of the limited rotating motion of coumarin inside the aquaphobic pocket of bovine serum albumin after encapsulation, the average $r(t)$ was enhanced to 1.7 ms.[151] The highest absorption and emission of coumarin in ethanol occurred at 435 and 532 nm, respectively. The blue shifting of the photoluminescence λ_{em} at 22 nm (from 532 nm to 510 nm) confirmed C153 encapsulation. The integral of overlap between the λ_{em} spectra of CDs & the absorption spectrum of C153 was 6.1×10^{15} mol^{-1} cm^{-1} nm^{-4}. The overlap between the λ_{em} and absorption spectra of coumarin and CNsAu was 6.55×10^{16} mol^{-1} cm^{-1} nm^{-4}. The C153 molecule interacted with the BSA protein's IIIA domain. The intensity of the emission increased as the [C153] increased from 0–3 μg mL^{-1} inside the (60 μg mL^{-1}) CNsAu. The PL intensity did not alter with increasing [C153], confirming that 60 μg mL^{-1} of CNsAu might absorb up to 3 μg mL^{-1} of C153. At 375 nm excitation, the decrement of CDs occurred in the existence of C153. The average lifespan of decay dynamics at 375 nm λ_{ex} and 440 nm λ_{em} was reduced from 10.6 ns to 5.4 ns owing to the transfer of energy from CDs to C153. At that λ_{ex}, a comparable quenching for C153-CNsAu composite was noticed. The energy-transfer from C153 to CNsAu reduced when the composite lifespan drops to 3.2 ns from 4 ns. At 375 nm λ_{ex} and 440 nm λ_{em}, the average lifespan of the CDs-C153-CNsAu composite dropped to 1.9 ns from 10.6 ns. A quicker component with a lifespan of 310 ps (a contribution of 77%) is detected. This quicker component was caused by energy-transfer from the CDs to the CNsAu *via* C153. The efficiency of energy transmission and the rate of energy transfer were 83% and 4.6×10^8 s^{-1}, respectively. Because of the chute energy transfer from CDs-CNsAu *via* C153, a bridge linker improved the efficiency.[152] The lifespan of CNsAu in the CDs-C153-CNsAu composite increased from 4.0 ms to 4.3 ms. C153 acted as a linker molecule because of its extremely extreme molar-extinction coefficient and good photodegradability.

6.1.3 Mechanism. The HOMO of the silane-capped CNsAu was determined using an electrochemical technique known as the Mott–Schottky method, which has been extensively used in the study of semiconductor electronic structures.[153,154] When exposed to visible light, O^{2-} radicals were produced. It was worth noting that $^{\bullet}O^{2-}$ was difficult to oxidize methylene blue because of their near redox potentials (−0.32 V for $O^2/^{\bullet}O^{2-}$) but was very susceptible to photo-induced electrons to produce H_2O_2, which was extremely oxidative. MB might react with the newly formed H_2O_2. The absence of the matching signal in EPR data indicated that –OH radicals were not involved in the process. Direct electron transfer between methylene blue molecules and CNs catalysts was possible because of the CNs's atom-level size, high proportion of shallow atoms, and efficient solvent dispersion.[155] As a result, photo-induced holes might easily form at the metal outside layer and get electrons completely from methylene blue molecules [Fig. 8].

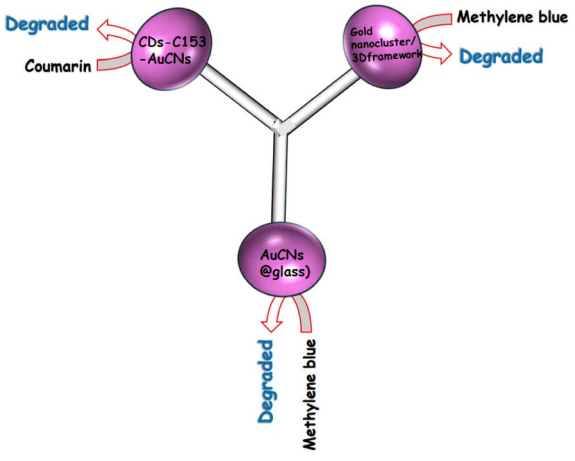

Fig. 7 Degradation of various dyes using CNsAu.

$$CNsAu + h\nu \rightarrow (CNsAu)^*$$

$$(CNsAu)^* + O_2 \rightarrow CNsAu(h^*) + {}^{\bullet}O_2^-$$

$${}^{\bullet}O_2^- + H_2O + (CNsAu)^* \rightarrow H_2O_2 + CNsAu(h^+)$$

$$CNsAu(h^+) + MB \rightarrow CNsAu + \text{oxidative products}$$

6.2 Copper nanocluster for dye degradation

6.2.1 Degradation of AB-B10. CNsCu were synthesized using the template-based method employing L-Cysteine (Cy) as a template. In the process, $CuSO_4$ was dissolved in an L-Cy solution and subsequently mixed with sodium hydroxide solution. The solution underwent incubation with stirring for four hours in a 55 °C water bath. For the preparation of CNsCu/C

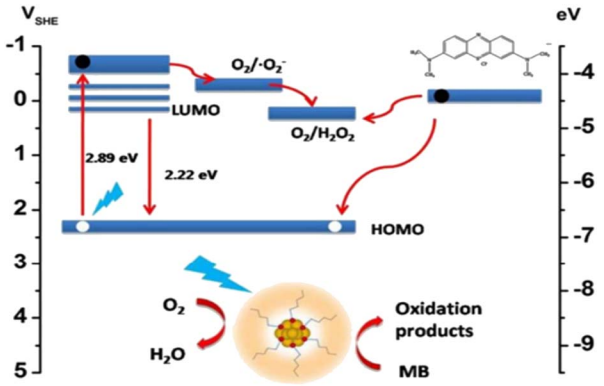

Fig. 8 Mechanism of the degradation of MB dye. Reproduced with permission from ref. 150, copyright 2024, *Nanoscale*.

composites, $CuSO_4$ was dissolved in an L-Cy solution, and this mixture was added to 0.5 g of carbon and stirred for five minutes. Following the addition of 0.4 mL of 1 M NaOH solution, the reaction was stirred in a 55 °C water bath for an additional 4.5 h. The CNsCu/C–H_2O_2 system was employed to degrade AB-B10, where CNsCu/C composite behaved as a Fenton-like catalyst.[87] The synergistic effect for degrading dye with CNsCu-based Fenton-like systems was investigated including five controls to degrade the AB-B10 solution: (1) H_2O_2 only, (2) CNsCu/C only, (3) $CuSO_4$ + H_2O_2, (4) CNsCu + H_2O_2, and (5) CNsCu/C (with a variable ratio) + H_2O_2. The degradation efficiencies of AB-B10 by independent H_2O_2 and the CNsCu/C system were both approximately 6%, indicating that H_2O_2 had a lower oxidation capacity than the hydroxyl group, and the elimination of AB-B10 by CNsCu/C only systems was mostly dependent on adsorption.[156] However, the AB-B10 solution varied from dark blue to light purple and could not attain a colorless state in the CNsCu + H_2O_2 Fenton-like system. CNsCu/C could be utilized to degrade AB-B10 across a wide pH range. The degradation of AB-B10 increased when [H_2O_2] increased from 5.0 to 25.0 mmol L^{-1}, indicating that [H_2O_2] could impact AB-10B degradation. However, when the [H_2O_2] was raised to 35 mmol L^{-1}, the degradation rate of the dye decreased. The reduction in process efficacy might be attributed to OH scavenging by excess H_2O_2.[157,158] CNsCu stability was preserved by encapsulating the carbonaceous matrix. Furthermore, the specific surface area might influence the catalytic performance. A smaller average pore size and a greater surface area & pore volume provided higher active sites for CNsCu/C, resulting in better catalytic efficiency than CNsCu.

6.2.2 Degradation of Rh-B. The photocatalytic activity was gauged by studying the degradation of Rh-B in an aqueous suspension under comparable conditions in the presence of air. 0.1% Na–$K_2Ti_6O_{13}$-Cu (Cu-NKT) showed superior activity for RhB degradation, with 87% degradation in 80 min of illumination, whereas 0.05% and 0.2% Cu-NKT showed 75.3% and 67.5% degradation, respectively, during the same irradiation duration. Cu-grafted Na–$K_2Ti_6O_{13}$ demonstrated improved activity.[159] The surface modification of sodium titanate with Cu(II) was important in increasing the photocatalytic activity of Na–$K_2Ti_6O_{13}$ because it allowed the generation of charge carriers *via* an interfacial charge transfer mechanism. When exposed to visible light, electrons were stimulated from the VB of Na–$K_2Ti_6O_{13}$ to the surface-grafted Cu(II) *via* interfacial charge transfer, resulting in the generation of h^+s in the VB of Na–$K_2Ti_6O_{13}$.[160]

6.2.3 Degradation of methylene blue. A blend containing $(NH_4)_6Mo_7O_{24}\cdot 4H_2O$, Cu $(NO_3)_2\cdot 3H_2O$, 4,4′-bpy, $C_2H_2O_4$, H_2O, and ethanol was stirred for 30 min in the presence of air. Subsequently, the suspension was heated at 160 °C for 5 days. The photocatalytic property of $(NH_4)_2CuMo_8O_{26}(C_{10}H_8N_2)_2$ (A) was evaluated by degrading the MB in the presence of UV light. Throughout the degrading process, the absorption of MB occurred at 665 nm. MB peaks were greatly reduced with the removal capacity reaching 80% for $(NH_4)_2CuMo_8O_{26}(C_{10}H_8N_2)_2$ after 1 h aging and just 12% for $Mo_8O_{26}(C_{10}H_{10}N_2)_2(C_5H_4N)_2(H_2O)_2$ after 1 h aging. As scavengers for OH$^\bullet$, superoxide ions, holes (h^+), BuOH-t (BAT), benzoquinone (QB), and ammonium oxalate (OA) were utilized as semiconducting materials. When BAT, QB, and OA were introduced into the photo-catalytic system, the associated degradation capacity reduced in varied degrees from 92% (with A) to 75% (with A + BAT), 44% (with A + QB), and 38% (with A + OA), respectively [Fig. 9].[161]

CNsCu were synthesized with MAT (3-amino-1,2,4-triazole-5-thiol) ligands, coupled with zinc(II) to produce a nano-sheet CNsCu-MOFs structure, resulting in AIE and improved PL intensity. Water molecules were introduced into S-CNsCu by the H-bond during aging in H_2O to enable 3D microflower structures, and weak phosphorescence was converted to strong fluorescence (30%) concurrently.[162] After drying, CNsCu released H_2O molecules, which were labeled with V-CNsCu and readily coupled with H_2O_2, which might be converted to radical $^\bullet$OH by copper(I). CNsCu-MOFs produced photogenerated e^- and h^+ when exposed to UV light. The as-obtained electrons reacted with H_2O_2 to produce additional radical OH, which was subsequently used to catalyze the dyes. The dyes also provided electrons to the remaining holes. The typical three dyes, MB,

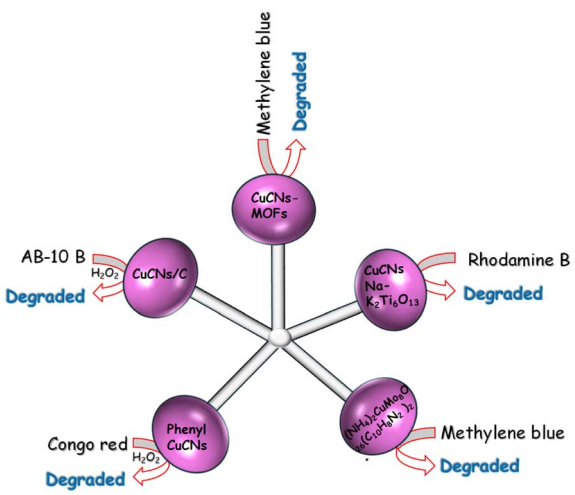

Fig. 9 Degradation of various dyes using CNsCu.

MO, and RB, as well as the antibiotic tetracycline, might be destroyed in 30 min, when exposed to an XL. Furthermore, in sunlight, the dye-antibiotic mixture might be destroyed after 100 min. V-CNsCu exhibited outstanding photo-Fenton catalytic activity and has promising photocatalytic potential in wastewater.

6.2.4 Degradation of Congo red (CR). Under photon exposure, phenyl-CNsCu exhibited selective removal of CR in water, showcasing rapid, efficient, and stable catalytic activity. In the presence of H_2O_2, phenyl-CNsCu gained additional electrons, expediting the decolorization of CR. These CNs demonstrated excellent antibacterial efficacy against both *E. coli* and *Staphylococcus aureus*. Importantly, even at high concentrations, phenyl-CNsCu proved to be non-toxic to normal cells (HL-7702) and malignant cells (HepG2), while effectively eliminating bacteria. Phenyl-CNsCu might serve as a promising nanomaterial for the selective breakdown of Congo red in aqueous solutions and as an adjunct for treating microbial infections.[163]

6.2.5 Mechanism. When exposed to visible light, e^-s were stimulated from the valence band of Na–$K_2Ti_6O_{13}$ to the surface grafted copper(II) (SGC) *via* interfacial charge transfer, resulting in the formation of a h^+ in the valence band of Na–$K_2Ti_6O_{13}$. Copper(II) was transformed into Cu(I) after grabbing an electron from the VB of Na–$K_2Ti_6O_{13}$, which might then pass the e^- to an O_2 to create reactive O_2 species *via* a multi-electron reduction process.[164] The SGC CNsCu, with a potential of 0.16 V *versus* SHE, might operate as an O_2 reduction site to generate OH radicals [Fig. 10].[160]

6.3 Silver nanocluster for dye degradation

6.3.1 Malachite green. Goswami *et al.*[165] used a visible light-emitting diodes (LED) light source to show the photo-catalytic behaviour of an organic semiconductor perylenetetracarboxylic acid (PCTA)-incorporated CNsAg in the degradation of MG dye.[166] CNsAg was produced using biocompatible captopril and PTCA as protective ligands. In the presence of $NaBH_4$, the dye's absorption maxima gradually decreased. However, without the catalyst, the rate of reduction of the dye by $NaBH_4$ was exceedingly sluggish. The percentage of decolorized dye in 45 min with $NaBH_4$ was only 20%, indicating the sluggish rate. The λ_{max} absorption of Malachite green was at 620 nm, which did not coincide with the absorption maxima of CNs (located between 400 and 500 nm). The size of the CNs also affected the photocatalytic effectiveness.[167,168] The photocatalytic activity of the so-produced CNsAg was assessed using a 50 W white LED light to decolorize a dilute aqueous solution ($\sim 10^{-5}$ M) of the dye. In the absence of the catalyst, white LED light caused minor photodegradation. Control photo-catalytic tests were also performed in the presence of PCTA, exhibiting little photocatalytic dye degradation. The catalyst-dye solution combination was held in the dark for 15 min to achieve desorption–adsorption equilibrium between the catalyst and the dye. The BH_4 ions might form a transient complex with the –CO in the –COOH group of captopril and PCTA, occupying the PCTA/CNsAg borders. Through the adsorption process, the MG dye was additionally attached to the CN's perimeter. The CNs worked as a relay for H^- ions, moving the ion to the malachite green molecule while simultaneously delocalizing e^-, as shown in the production of Leuco MG. For scavenging, aqueous solutions of AA and ethylenediaminetetraacetic with isopropanol and glycerol were utilized. The addition of glycerol, which was widely recognized as a highly effective hole and $^{\bullet}OH$ scavenger, resulted in the slowest rate of elimination. This means that the most active species in the degradation process were hole and $^{\bullet}OH$.

A class of hybrid nanomaterials was developed by attaching CNsAg with TiO_2/Nb_2O_5 (Ag/T/N) nanocomposite. It was found that a two-step synthetic technique successfully decorated T/N with CNsAg, whereas a one-step synthesis generated T/N CNs that had minimal Nb_2O_5 content. When CNsAg were attached to TiO_2/Nb_2O_5, the photo-catalytic activity of the nanocomposite for the elimination of MG was increased as compared to the same materials with insignificant Nb_2O_5 content. The addition of Nb_2O_5 to a hybrid nanocomposite allowed for the selective improvement of MG photocatalytic degradation. It indicated the importance of transition metal ions in the removal of MG. The dye was eliminated in half an hour in the dark using Ag/T/N as a catalyst. It suggested dye adsorption with the catalyst, which might be related to the dye's strong intermolecular interaction with the hybrid nanocomposite. The excessive quantity of Nb_2O_5 loading in the hybrid nanocomposite catalyst might increase the surface acidity of the catalyst, favoring the degradation of cationic dyes like Malachite green. The suspension was exposed to visible light after adsorption and desorption, and fast elimination of the dye was observed. The usage of Ag/T/N resulted in increased visible light absorption. Exposure to visible light produced more e^-–h^+ pairs. Recombination rates in hybrid nanocomposites were lowered due to the existence of ternary junctions and a larger range of band-gaps. This process resulted in enhanced photocatalytic degradation. The photocatalytic activities of the catalyst were determined by estimating the dye absorbance after photodegradation.[169]

6.3.2 Methylene blue. $AgNO_3$ was combined with an aqueous solution of L-His under stirring at room temperature. Almost instantly, white-colored silver-L-His complexes were formed. Following a 10 min interval, 0.0050 mL of an NaOH solution was introduced into the solution, which was then exposed to UV light at 254 nm for 1 h. The CNsAg-L-His was produced using a surface sol–gel technique to generate

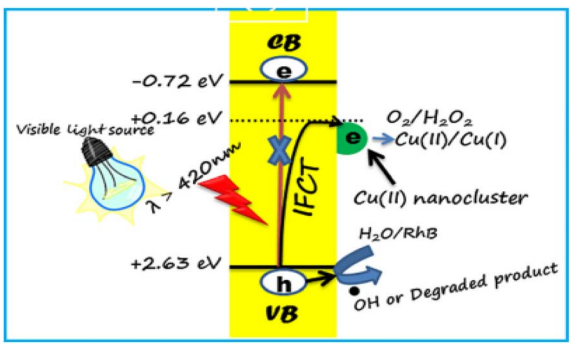

Fig. 10 Mechanism of dye degradation using CNsCu. Reproduced with permission from ref. 160, copyright 2024, *Mater. Lett.*

a photocatalyst. MB has significant optical absorption in the 500–700 nm region. In the absence of a catalyst (CNsAg-L-His@Al_2O_3@TiO_2), the photo-degradation of MB by sunlight exposure failed. The reaction kinetics of MB photodegradation in the existence of the Ag@Al_2O_3@TiO_2 photocatalyst showed a decrease in the MB absorbance at 665 nm. Under visible-light exposure, the photocatalytic efficiency of the CNsAg-L-His@Al_2O_3@TiO_2 photocatalyst was significantly greater than that of the other photocatalysts. Due to their wide band-gap energy (>3 eV), pure TiO_2 and β-Al_2O_3 had limited photocatalytic activity. When the initial [MB] was raised from 10^{-5} to 10^{-4} M, the degradation rate was reduced by about 30%. Because of the greater dye concentration, a portion of the incoming photons might have been blocked by extra free dye molecules. Photons were available for interaction with the photocatalyst and adsorbed MB surface. The generation of reactive hydroxyl and superoxide radicals was predicted to be greatly reduced, hence inhibiting the process.[170]

$AgNO_3$ was thoroughly ground with mercaptosuccinic acid (H_2MSA), resulting in an orange-peel-colored powder (silver thiolate), which was further ground with $NaBH_4$, producing a brownish powder. After the addition of distilled water to this suspension, the dark-colored solution was the final product. The embedment of [$Ag_9(H_2MSA)_7$] on graphitic carbon nitride nanosheets (GCN) produced extended visible-light absorption *via* multiple single–electron transitions in the silver quantum cluster (AgQCs) and an effective electronic structure for $OH^{\bullet}$ radical generation, allowing for enhanced efficacy in the photocatalytic elimination of MB and MO in comparison to pristine GCNs and AgPNls@GCN. Bootharaju and Pradeep[171] recently showed that ligand-protected AgQCs might exclusively eliminate cationic dyes due to a favorable electrostatic interaction (between dye molecules and CNs). Due to significant electrostatic repulsion between anionic dye molecules and AgQCs, the removal of anionic dye molecules was a failure. Both types of dyes were utilized as model contaminants to isolate the adsorptive behavior of AgQCs from the photocatalytic activity. The photoelimination of blue dyes by AgQCs-GCN was roughly three times quicker than that of orange dyes owing to electrostatic interaction among sulfur atoms in blue dye molecules and AgQCsCNs. MO and AgQCs exhibited substantial electrostatic repulsion. The sulfonic group of MO had a high electronegative core and was more electron-withdrawing than the carboxylic groups found in AgQCs. The adsorption value was low, which significantly lowered the photo-elimination rate. AgQCs-GCN was a linked semiconductor composite that created a semiconductor heterojunction due to differences in the CB & VB redox energy levels, which enhanced charge carrier separation. The substantial quantum confinement effect in AgQCs allowed it to display many molecular-like single–electron transitions.[172,173]

The catalytic properties of MOFs could be improved by including metallic species in their porosity post-synthetically. MOFs could be employed to stabilize PNlsM of variable size inside their porosity due to their unusually large surface area and well-defined porous structure *via* the photo-reduction approach for the CNsAg on a photoactive porous Ti-carboxylate MIL-125-NH_2 MOF. The robust MOF interaction among the amino group & silver atoms promoted CNsAg evolution, resulting in the efficient surfactant-free catalyst CNsAg@MIL-125-NH_2 with an increment of visible light absorption. The photo-elimination of the emerging organic contaminants (OECs) MB and sulfamethazine (MST) in water treatment, as well as the catalytic hydrogenation of 4-NA to *p*-phenylenediamine (PDP), were examined. It was worth noting that as compared to the MIL-125-NH_2, the composite exhibited enhanced catalytic activity and stability, being able to photodegrade 92% of MB in 1 h, 96% of MST in half an hour, and 100% of 4-NA to PDP in half an hour. CNsAg@MIL-125-NH_2 photodegraded up to 72 ± 4 and 92 ± 3% of the dye in the solution in only 10 min and 1 h, respectively. The rapid dye elimination kinetics was most likely attributed to (i) the lower energy band gap induced by the CNsAg plasmon resonance (2.5 and 2.6 eV for CNsAg@MIL-125-NH_2 and MIL-125-NH_2, respectively);[174] (ii) the reduction of the e^-–h^+ recombination as CNsAg worked as the e^- trapping agent and (iii) the chemical affinity of Ag to the sulfur and nitrogen atoms of the MB structure.[175] After 1 h in the dark, CNsAg@MIL-125-NH_2 absorbed 70% of the dye whereas the pure MOF only removed 40%.[176]

The strong electrostatic adsorption (SAE) approach was used to deposit monodispersed bare CNsAg with a particle size of 1.3 nm inside the pores of a TiO_2-modified mesoporous Mobile Composition of Matter No. 41 (MCM-41). The photocatalytic degradation of MB dye under visible light irradiation was used to assess the performance of the photocatalysts. After 2 h of exposure to TiO_2/Ag/MCM-41 (SAE) photocatalyst, about 100% decolorization of 50 000 ppb MB solution was observed. The SAE catalyst's exceptional performance was ascribed to CNsAg that were uniformly scattered throughout the mesopores of MCM-41, resulting in more silver surface sites accessible for the catalytic reaction.[177]

6.3.3 Rhodamine B. The synthesis and structural characterization of a giant 102-CNsAg denoted as 1 is given here. According to a single X-ray structural investigation, 1 had a multi-shelled metallic core of Ag_6*Ag_{24}*Ag_{60}*Ag_{12}. A truncated octahedral Ag_{24} shell surrounded an octahedral Ag_6 core. Most significantly, the Ag_{24} shell was made up of hitherto noticed sodalite-type Ag orthophosphate CNs, which was like the well-known silver phosphate photocatalyst. The Ag orthophosphate CNs were covered by 6-interstitial S^{2-} atoms, resulting in a unique anionic CNs [Ag_6*$(Ag_3PO_4)_8S_6$]$^{6-}$ that served as a complex polyhedral template, with ample surface oxygen and sulfur atoms driving the formation of a rare rhombicosidodecahedral Ag_{60} shell. The elimination of Rh-B under visible-light irradiation (>420 nm) indicated that 1 might be a possible narrow band-gap semiconducting material. After 40 min of irradiation, 1 decreases the Rh-B content by 85%. A blank experiment, for contrast, reveals that the photolysis of Rh-B solution was insignificant in the absence of 1, omitting the self-photolysis of the Rh-B dye. The cluster's stability might be checked by comparing the IR and UV/Vis spectra. 1 had photocatalytic activity equivalent to Au_{23}(S-

Adm)$_{15}$ (HS-Adm = adamantanethiol) CNs, which destroyed the RhB dye by 83% after 40 min of visible-light irradiation.[178,179]

A low-temperature approach was employed for the production of titanium dioxide-functionalized CNsAg ligated with GSH. CNsAg alone exhibited little visible light photocatalysis, whereas the addition of extreme-trivial titania decreased the band gap of the hybrid CNs and facilitated solar activation, resulting in increased catalytic activity. The elimination of Rh-B revealed the visible light-driven catalytic capability of hybrid CNs. Density Functional Theory (DFT) simulations were utilized to investigate the interaction of surface ligands with titanium dioxide molecules using simple structural models Ag(SCH$_3$)$_n$–TiO$_2$. The absorption spectra of Rh-B solution complied with visible light exposure utilizing TiO$_2$–Ag hybrid CNs as a nanocatalyst at regular time intervals.[180] There was a gradual decrease in the absorbance of the peak centered at 550 nm. When photo-catalyzed utilizing CNsAg as a catalyst, there was no discernible change in the absorption spectra of the dye solution. CNsAg were crucial for the solar activation of TiO$_2$ CNs molecules. The introduction of TiO$_2$ (10.8% Ti) significantly improved the visible light-induced photocatalytic activity of CNsAg. The hybrid nanocluster's increased photocatalytic activity could be attributed to decreased e^--hole pair recombination. Metal–metal and metal–ligand interactions shift the absorption band to the visible range, enabling visible light photocatalysis. The photocatalytic activity of PNls was determined by their size, shape, and crystal structure.[181,182]

The physical characteristics and photocatalytic activities of CNsAg-encumbered graphitic carbon nitride (C$_3$N$_4$-g) nanosheets were investigated. The accumulation of CNsAg on the surface of C$_3$N$_4$-g nanosheets changes the crystal structure and reduces the band-gap energy of C$_3$N$_4$-g. The dramatic drop in intensity indicates that C$_3$N$_4$-g@Ag heterojunctions efficiently avoid photo-generated e^-–h^+ recombination. The elimination of Rh-B under XL was used to expose the photocatalytic activity of photocatalysts. The increased absorbance in CNsAg occurred due to the SPR effect,[183,184] suggesting that it will contribute to RhB degradation. The photocatalytic capabilities of C$_3$N$_4$-g and GCN/Ag samples degraded RhB under XL exposure. The elimination rate of dye was indirectly by varying the intensity of the 554 nm absorption peak of RhB solution using a standard curve linking [RhB] to absorbance. After 50 min of XL irradiation, the 554 nm absorption peak of Rh-B not only vanished but also changed from 554 nm to 530 nm, revealing the disintegration of RhB's conjugated structure. The increase in the photocatalytic activity in photogenerated electrons on C$_3$N$_4$-g nanosheets could be effectively transferred to CNsAg, which decreases the rate of e^- and h^+ recombination. The intensity of PL was also reduced. UV-vis analysis and the interpretation of CT$_{SPR}$ may have contributed to this significant rise in photocatalytic activity.[185]

The Ag/g-C$_3$N$_4$ composite (CN-sr@Ag) was enhanced by chemical reduction using ultrasonic spray technology. This technique minimized the aggregation of C$_3$N$_4$-g nanosheets and induced a micron-scale reaction, resulting in uniform distribution and size reduction of CNsAg. The reaction rate constant for RhB degradation was 0.0322 min^{-1}, which was approximately 3 and 7 times greater than that of the Ag/CN composite made using the standard chemical reduction technique (Ag/CN-cr) and bare C$_3$N$_4$-g nanosheets. In 100 min, the [RhB] was reduced by up to 96.47% over a CN-sr@Ag catalyst, whereas it was eliminated by 65% and 43% in the presence of CN-cr@Ag and CN, respectively. The absorption spectra of RhB were at 554 nm. The distinctive absorption spectra of Rh-B at 554 nm decreased rapidly, suggesting that RhB was steadily destroyed as the reaction time increased. The highest absorption site displayed minor hypsochromic changes, which were ascribed to the generation of *N*-demethylated intermediates of Rh-B during photo elimination. The TEM images of CN-sr@Ag before and after deterioration show that the average size of CNsAg on the surface of CN did not change much after usage (from 15 to 17 nm), but there was aggregation and a wider size distribution range. The Ag content in the composite increased from 3.5 to 3%. The photocatalytic performance of CN-sr@Ag was lowered due to the inevitable agglomeration and loss of silver species. Except for a slightly larger primary peak, the XRD patterns of the CN-sr@Ag samples before and after degradation demonstrate that the peak shape and position were nearly intact.[186]

A CeO$_2$/Ag nano-structured material with photocatalytic and antibacterial properties was developed utilizing a simple solution combustion synthesis (SCS) technique with tartaric acid as a fuel. Under UV irradiation, CeO$_2$–Ag materials were used as photocatalysts for the catalytic elimination of Rh-B dye in 150 min. RhB showed an absorbance peak at 554 nm. The photodegradation of Rh-B *versus* the quantity of CeO$_2$/Ag clearly showed that the elimination of Rh-B dye increases with an increase in the amount of catalyst from 100 to 150 mg and subsequently decreases with an increase in the quantity of CeO$_2$/Ag of 200 mg. As a result of the intense redox interaction,[187] dye molecules might get adsorbed on the active sites of the CeO$_2$/Ag nanostructured materials. The decrease in catalytic performance with increasing catalyst quantity was thus thought to be attributable to the coarsening of nanoparticles. Kumar and Pandey[188] also discovered light scattering, which damages the photocatalyst's catalytic capabilities. It was discovered that CeO$_2$ nano-flakes demonstrated 60% dye degradation in 150 min. The antibacterial activity of Ag/CeO$_2$ nanostructured materials against Gram-positive (*S. aureus*) and Gram-negative (*P. aeruginosa*) bacterial strains was also obtained [Fig. 11].[189]

CNsM based on Au as core and Ag as shell, named CNsAu@Ag, were electro-statically associated with functionalized semiconducting MoS$_2$ nanosheets named MoS$_2$-f. The Rh-B photo-degradation catalyst CNsAu@Ag/MoS$_2$-f was used for wastewater cleansing from organic contaminant dyes. CNsAu@Ag/f-MoS$_2$ produces extremely reactive hydroxyl radicals by reducing oxygen from charge-separated photogenerated electrons, resulting in superoxide radical ions. The h^+ on CNsAu@Ag degraded Rh-B molecules, resulting in a decolorized magenta solution and loss of the distinctive absorbance at 554 nm. Without a catalyst, no changes were shown in RhB, demonstrating that light irradiation alone was insufficient to destroy Rh-B. Similarly, the UV-vis spectra of Rh-B remained virtually unchanged in the existence of solely f-MoS$_2$ (*i.e.*,

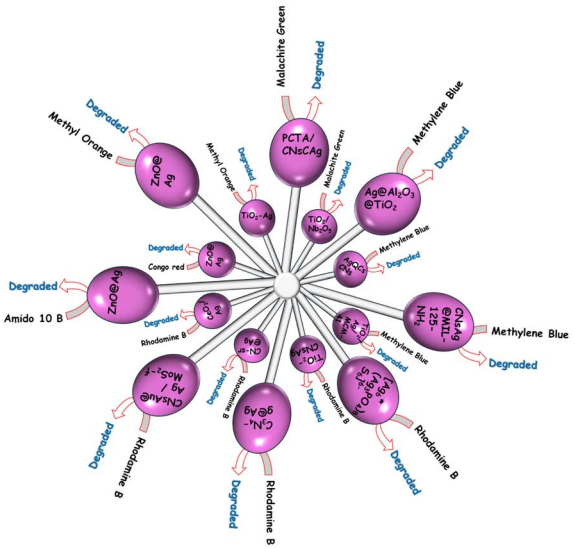

Fig. 11 Degradation of various dyes with CNsAg.

without any CNsAu@Ag). When a catalytic quantity of bare CNsAu@Ag was applied, the absorption band of Rh-B gradually diminished as time passed, suggesting RhB breakdown. After 180 min of irradiation, the absorption band blue-shifted by 12 nm, resulting in about 70% degradation of Rh-B. The addition of CNsAu@Ag/MoS_2-f resulted in virtually quantitative elimination of Rh-B (>85%) in 100 min, which was somewhat longer than the half-time recorded for CNsAu@Ag. Furthermore, after 210 min of light irradiation, RhB degradation was found in CNsAu and CNsAg at about 60 and 50%, respectively. It showed that coinage metal itself was not sufficient for the degradation of dye. The synergism of coinage metal nanocluster was also not able to degrade the dye without the transition metal. Transition metal-capped coinage metal nanoclusters for dye degradation play a vital role.[190]

6.3.4 Amino 10 B (AB-10 B). Amido black 10B dye showed a degradation pattern, and hybrid Ag@ZnO nanorods had better catalytic activity than ZnO nanorods. The AB-10B dye degradation process showed that photogenerated h^+ was liable for the oxidative route, which was followed by an irreversible enduring mineralization phase. Under UV irradiation, 50% dye degradation was observed in 26 min for ZnO while for the Ag@ZnO hybrid, it was 12 min due to the improved photocatalytic action of its hybrid core–shell nanostructure.[191] The deterioration pattern of hybrid Ag@ZnO was quicker in solar-irradiated samples than in ZnO nanorods, showing the synergism effect of transition metal nanoparticle with coinage metal nanocluster in both exposure samples and showed the plasmonic behaviour of coinage metal (Ag) nanocluster.[192]

6.3.5 Congo red (CR). The elimination of CR could be achieved, when exposed to UV and solar light. Due to the photogenerated holes, an oxidative route by Congo red dye was formed, culminating in the mineralization process and the formation of carbon dioxide, water, nitrate, NH_4^+, and sulfate. The catalytic activity of Ag@ZnO core–shell nanorods was significantly higher than that of zinc oxide nanorods, showing the influence of CNsAg. In UV light, 50% degradation was shown in 12 min for the hybrid Ag@ZnO nanorods. In solar light, a similar quicker degradation process was observed for the hybrid Ag@ZnO than ZnO nanorods, indicating the synergism effect of transition metal nanoparticle with coinage metal nanocluster in both exposed samples and showed the plasmonic behavior of the coinage metal (Ag) nanocluster.[192]

6.3.6 Methyl orange. Emerging contaminants (ECs) are a diverse group of substances that are not usually eliminated from wastewater using traditional procedures, posing health and environmental concerns. Titanium dioxide and zinc oxide are the most common inorganic photocatalysts owing to their inexpensive cost and widespread accessibility. Tiny levels of CNs might result in increased light absorption and a reduction in the recombination rate of e^-/h^+ pairs, showing better photocatalytic activity. CNsAg was placed on ZnO PNls (Ag@ZnO) to evaluate their catalytic activity under both ultraviolet A (UVA) and visible light. As the most effective photocatalyst, Ag@ZnO with 1.3% (w/w) silver was chosen. The impact of [Ag@ZnO] was observed in aqueous samples with an initial [orange II] 10 mg L^{-1}, which were then exposed to white light with 0.2–1 g L^{-1} of ZnO PNls or Ag@ZnO (1.3%) CNs, and UVA light with 0.05–0.5 g L^{-1} of photocatalyst.[193]

Photo Fenton Process (FPP) for UV-light elimination of Methyl Orange (MO) utilizing UV/H_2O_2/Fe^{2+} & TiO_2-modified photocatalyst with Ag deposition (TiO_2-Ag). The rate of kinetics of TiO_2-Ag demonstrated greater catalytic performance than FPP since the elimination of the dye took just an hour using TiO_2-Ag but it took 2 h for TiO_2 using FPP. Because of the plasmon resonance effect of e^- transfer from the shallow of TiO_2 over metallic Ag at nanoscale particulate sizes, Ag-metalized titanium dioxide photocatalyst had a high surface area and particles were greatly impacted electronically under UV light.[194]

6.3.7 Mechanism. To attain Fermi energy level equilibrium (E_f), e^- migrates from a transition metal to the conduction band of Ag because the transition metal's Fermi energy level is higher than that of Ag's. Irradiating transition metal@Ag core–shell nanorods with >energy than the band gap energy results in the promotion of an e^- from the VB to the CB, leaving a h_{vb}^+ in the valence band.[195,196] Potential energy could promote the transport of e_{cb} (photoelectrons) from a transition metal to Ag. CNsAg acts as an electron sink, diminishing the amount of photoinduced electrons and holes to recombine while also prolonging the lifetime of photogenerated pairs and attracting them to the surface of the particle. When electrons (e_{cb}^-) were injected into the surface, they were scavenged by the adsorbed O_2 molecule, resulting in the creation of an $^{\bullet}O^{2-}$, while h_{vb}^+ produced at the VB react with surface-bound OH and H_2O to form hydroxyl and hydroperoxyl radicals [Fig. 12].[192]

7. Adsorption of dye

Adsorption is a well-established technology for dye removal from wastewater due to its simplicity and cheaper cost when compared to other methods. The development of adsorbents from diverse biomass wastes as a replacement for commercial

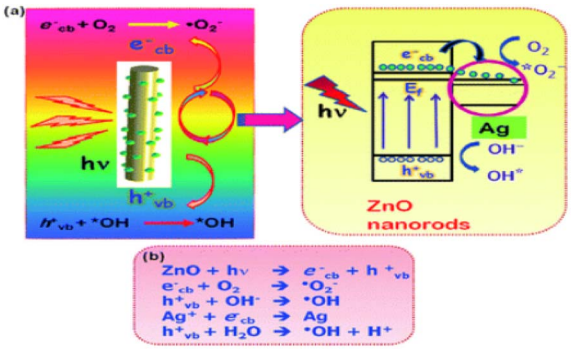

Fig. 12 Mechanism of the degradation of dyes. Reproduced with permission from ref. 192, copyright 2024, *RSC Advances*.

activated carbons improves the economic effectiveness of the process.[197]

7.1 Rhodamine B

A modified solid-state approach was employed to synthesize an atomically accurate, dithiol-coated CNsAg known as $(DMSA)_4$-Ag_7 (DMSA: meso-2,3-dimercaptosuccinic acid). The CNs exhibited molecular visual absorption characteristics, featuring a significant peak at 500 nm. In comparison to PNls coated with ligands such as citrate and mercaptosuccinic acid (MSA) and possessing similar chemical structures to DMSA, these clusters displayed significantly higher efficacy for dye removal. The superior dye elimination efficiency of CNs could be attributed to their trivial size, larger shallow area, and favorable electrostatic interactions with cationic dyes. Clusters demonstrated remarkable dye removal performance, absorbing over 80% in 10 min and 99.7% in 15 min, whereas bare alumina adsorbed only about 23% in the same duration. This underscored the highly favourable capability of supported CNs for the elimination of dyes like R-6G. The change in the intensity of dyes corroborated the adsorption of R-6G on CNs. Such CNs, featuring RCOO– groups, exhibited a destructive zeta-potential (PZ) of 75.7 mV, while R-6G maintained a nearly neutral charge (0.1 mV). Upon adding R-6G to the CNs, a reduction in the PZ of the CNs to 57 mV occurred at room temperature, indicating charge neutralization due to electrostatic attraction among oppositely charged ions. The XPS analysis of R-6G-treated supported clusters demonstrated a consistent Ag $3d_{5/2}$ peak at 368.1 eV associated with Ag^0 in supported clusters, confirming that R-6G uptake was primarily due to adsorption. R6G, MB, MR, and MO had uptake capabilities of 17.2, 16.5, 3.1, and 0.2 mg g^{-1} of the cluster, respectively.[198]

The SCN^- reduction process in colloidal gold solutions results in CNs with a diameter of 2–3 nm. These particles were too tiny to show any surface plasmon absorption characteristics. The introduction of R-6G into colloidal Au solution altered the absorption spectrum significantly. Intermolecular and intercluster interactions were induced by the dye molecules on the Au surface. Furthermore, dye adsorption on AuNPI caused charge neutralisation on the surface, leading the dye/Au assembly to coalesce. The absorbance at 525 nm decreased when the [dye/Au] ratio increased. The monomeric absorption band at 525 nm faded at a [dye/Au] ratio of 11.7, and two additional bands at 507 and 537 nm arose. While a similar amount of SCN^- was introduced into an R-6G solution, no similar absorption changes were detected. The robust electrostatic interaction among the dye molecule and the negatively charged SCN@Au was responsible for these absorption variations. These aggregation effects were dominant because the dye molecule was tightly packed around the metal body causing intermolecular interactions [Fig. 13].

A herringbone-type aggregation of dyes could not be ruled out. H-type aggregation represented a sandwich-type stacking of dye molecules around AuNPls. The Au colloids formed *via* thiocyanate reduction were exceedingly tiny, with particle diameters ranging from 2 to 3 nm.[199] AuNPls linked to R-6G had comparable particle diameters but existed as dense CNs. The laser-irradiated particles had a comparatively wide diameter of 5–20 nm. During the laser irradiation in Rh-6G/Au CNs' fabrication, larger-sized particles were obtained when AuNPls transformed into tiny aggregated CNs (the laser-induced fusion process).[200]

8. Sensing of dye with coinage metal nanocluster

Nanosensors utilize PNls recognition sites for selection and signal transduction, indicating the presence of contaminants. Sensing devices are designed to detect a single analyte or a group of analytes at the same time, a concept known as multiplexity [Fig. 14].[201]

Fluorescence resonance energy (FRE) transfer is a non-radiative energy transfer procedure that uses long-range dipole–dipole coupling to transmit energy from an excited state donor to a nearby ground state acceptor.[202] Organic fluorophores,[203] fluorescent proteins,[204] and quantum dots[205] have all been used to build the FRE transfer assay [Table 2].

Chen *et al.*[206] demonstrated that FRE transfer among Sudan 1 to 4 & polyethyleneimine-capped (EIP-CNsAg) that were lesser than the critical size for electric resources quantisation (2 nm) were studied and then used for Sudan 1 to 4 sensing in ethanol.

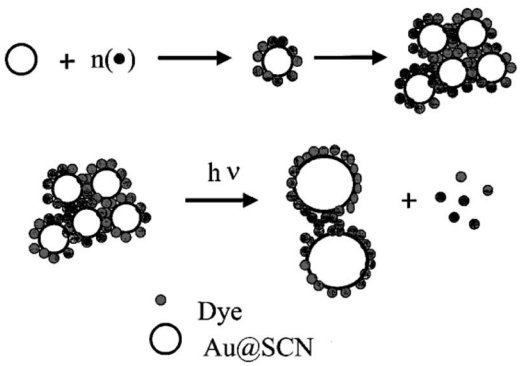

Fig. 13 Systematic diagram of dye adsorption. Reproduced with permission from ref. 200, copyright 2024, *J. Phys Chem. B*.

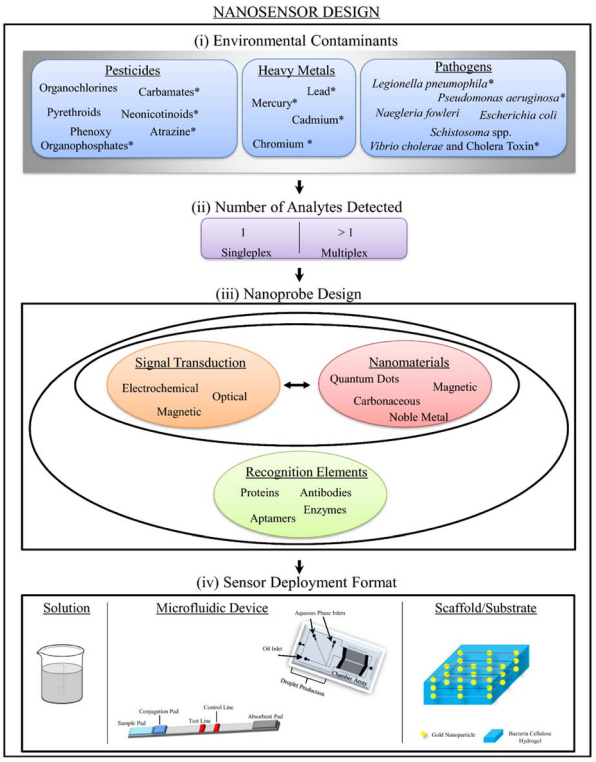

Fig. 14 Schematic illustration of nanosensor design, including ambient contaminants, detected analytes, probe design, and deployment format. Reproduced with permission from ref. 201, copyright 2024, *J. Nanobiotechnol.*

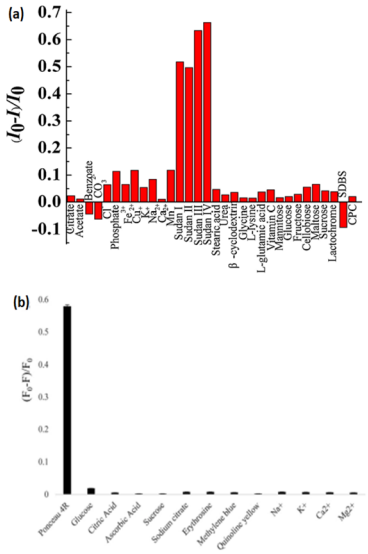

Fig. 15 Bar diagram of sensing of dyes. Reproduced with permission from ref. 206 copyright 2024, *Sens. Actuators, B*; Reproduced with permission from ref. 207 copyright 2024, *Journal of Photochemistry and Photobiology A: Chemistry*.

When stimulated at 375 nm, the PEI-AgCNs showed significant blue fluorescence, which was substantially amplified when the CNs were dissolved in specified organic solvents, particularly *n*-propanol and ethanol. The fluorescence of PEI-CNsAg could be effectively diminished by the addition of Sudan dyes. The solvatofluorochromic properties of EIP-capped CNsAg caused the centered wavelength of 455 nm in water to shift to 450 nm in ethanol. In the concentration range of 5–50 μL mL^{-1}, a good linear connection between emissive intensity and [EIP-CNsAg] was established. However, the fluorescence response deviated from linearity. In the presence of Sudan I–IV at a concentration of 10 μL mL^{-1}, a lower concentration fluorescence probe was shown to have greater quenching efficacy. Sudan I and II quenching efficiencies nearly remained constant with rising temperatures; however, Sudan III and IV quenching efficiencies at higher temperatures were larger than those at lower temperatures [Fig. 15].

CNsCu were developed using a one-pot hydrothermal reaction between Cu and L-Cy (reductant and capping agent). The influence of pH, incubation duration, and temperature on CNsCu emission signals was observed. The introduction of Ponceau-4R to the CNs solution caused fluorescence quenching, and the probable quenching mechanism was static quenching. In the existence and absence of Ponceau-4R, λ_{em} & λ_{ex} were 470 & 375 nm, respectively. The increased addition of L-Cy could increase the rate of Cu^{2+} reduction, resulting in the production of massive CNs. When the amount of L-Cy was too low, the degree of reduction was inadequate, resulting in poor stability and CNsCu agglomeration. CNsCu had a carboxyl group on their surface, whereas Ponceau-4R contained three RSO_3H. Because both RSO_3H and O_2 atoms on the surface of –COOH group were electronegative, these interactions led to the formation of a complex among Ponceau-4R and CNsCu. The interaction of these two groups and the formation of H-bonds effectively suppressed the fluorescence intensity of CNsCu. Complex molecules generated between the emitter and quencher altered the luminescence property. The blue shift in the λ_{em} of CNsCu suggested the altered size. The size of generated CNsCu was 3.3 nm, but after reaction with the dye, it was 17.4 nm, according to dynamic light scattering.[207]

9. Future prospective & conclusion

Copper nanoclusters have brilliant colors and nearly constant energy levels. Quantum confinement results in a distinct photoluminescence property in CNs including CNsAu, CNsAg,

Table 2 Coinage CNsM with different capping agents with various properties for sensing applications

Nanocluster	*hv*	$\lambda_{ex}/\lambda_{em}$	UV (nm)	Size	Oxidation state
Silver nanocluster	Hyperbranched polyethyleneimine	375/450	365	~2 nm	0
Copper nanocluster	L-Cysteine	375/450	375	3 nm	0

CNsCu, and CNsPt. Coinage metal nanoclusters with transition metals play a vital role in dye degradation because the addition of transition metal with the coinage metal nanocluster increases the surface-to-volume ratio of the nanoclusters. Increasing the surface volume is responsible for the photocatalytic degradation and adsorption behavior of the dye. Colored discharge, particularly dyes from industry, endangers the environment and harms aquatic and human life. Organic dyes are widely utilized as colored chemicals in a variety of sectors, including textiles, paper, cosmetics, leather, and food. For the formation of copper nanocluster, different capping agents were used. Copper nanocluster with transition metal shows an interestingly synergistic effect. In the presence of synergism behavior, the change in nanoclusters' behavior for dye degradation was shown in this review article. Many literature showed the effect of H_2O_2 on dye degradation. In the overall review article, we showed that in the presence of gold nanoclusters, the time consumption for degradation is lower than that of other metals. Few studies are available on the degradation in copper and gold nanoclusters in comparison to silver nanoclusters. Coinage metal nanoclusters do not show any degradation without doping/alloying with the transition metals. It shows the vital role of synergism behavior on dye degradation. Dye degradation, adsorption, mechanism, and sensing are shown in this review article. It will hopefully be an asset to young researchers, venturing into the field of environmental nanoscience to cope with recent challenges in the environment.

Conflicts of interest

There is no conflict of interest.

Notes and references

1 Y.-H. Chiu, T.-F. M. Chang, C.-Y. Chen, M. Sone and Y.-J. Hsu, *Catalysts*, 2019, **9**, 430.
2 I. K. Konstantinou and T. A. Albanis, *Appl. Catal., B*, 2004, **49**, 1.
3 F. Deng, L. Min, X. Luo, S. Wu and S. Luo, *Nanoscale*, 2013, **5**, 8703.
4 S. Xu, Y. Zhu, L. Jiang and Y. Dan, *Water, Air, Soil Pollut.*, 2010, **213**, 151.
5 D. Wang, Y. Wang, X. Li, Q. Luo, J. An and J. Yue, *Catal. Commun.*, 2008, **9**, 1162.
6 A. Kumar and G. Pandey, *Mater. Sci. Eng. Int. J.*, 2017, **1**, 1.
7 M. A. Brown and S. C. De Vito, *Environ. Sci. Technol.*, 1993, **23**, 249.
8 S. Chen, J. Zhang, C. Zhang, Q. Yue, Y. Li and C. Li, *Desalination*, 2010, **252**, 149.
9 N. Daneshvar, D. Salari and A. Khataee, *J. Photochem. Photobiol., A*, 2003, **157**, 111.
10 S. Ledakowicz and M. Gonera, *Water Res.*, 1999, **33**, 2511.
11 J. Grzechulska and A. W. Morawski, *Appl. Catal., B*, 2002, **36**, 45.
12 A. Wahab, *Appl. Nanosci.*, 2019, **9**, 1823.
13 I. Kanelidis and T. Kraus, *Beilstein J. Nanotechnol.*, 2017, **8**, 2625–2639.
14 J. P. Chinta, *Sens. Actuators, B*, 2017, **248**, 733–752.
15 P. Sharma and M. Ganguly, *IJEST*, 2023, 1–20, DOI: **10.1007/s13762-023-05171-6**.
16 H. Si, T. Shu, X. Du, L. Su and X. Zhang, *Biosensors*, 2022, **12**, 511.
17 A. Henglein, *J. Phys. Chem.*, 1993, **97**, 5457.
18 P. Mulvaney, M. Giersig and A. J. Henglein, *Phys. Chem.*, 1993, **97**, 7061.
19 L. M. Liz-Marzán, M. Giersig and P. Mulvaney, *Langmuir*, 1996, **12**, 4329.
20 A. Haesselbarth, A. Eychmueller, R. Eichberger, M. Giersig, A. Mews and H. Weller, *J. Phys. Chem.*, 1993, **97**, 5333.
21 U. Kreibig and M. Vollmer, *Optical Properties of Metal Clusters*, Springer, Berlin, 1995.
22 R. G. Freeman, M. B. Hommer, K. C. Grabar, M. A. Jackson and M. J. Natan, *J. Phys. Chem.*, 1996, **100**, 718.
23 A. Martino, S. A. Yamanaka, J. S. Kawola and D. A. Loy, *Chem. Mater.*, 1997, **9**, 423.
24 G. L. Hornyak, C. J. Patrissi and C. R. Martin, *J. Phys. Chem. B*, 1997, **101**, 1548.
25 B. Shanghavi and P. V. Kamat, *J. Phys. Chem. B*, 1997, **101**, 7675.
26 P. V. Kamat, Composite Semiconductor Nanoclusters, in *Semiconductor NanoclusterssPhysical, Chemical and Catalytic Aspects*, ed. Kamat, P. V. and Meisel, D., Elsevier Science, Amsterdam, 1997, vol. 237.
27 A. Henglein, *Chem. Mater.*, 1998, **10**, 444.
28 G. Li and R. Jin, *Acc. Chem. Res.*, 2013, **46**, 1749–1758.
29 W. T. Wallace, R. B. Wyrwas, R. L. Whetten, R. Mitric and V. Bonacic-Koutecky, *J. Am. Chem. Soc.*, 2003, **125**, 8408–8414.
30 S. Kumar and R. Jin, *Nanoscale*, 2012, **4**, 4222–4227.
31 G. Schmid, *Chem. Soc. Rev.*, 2008, **37**, 1909–1930.
32 K. Saha, S. S. Agasti, C. Kim, X. Li and V. M. Rotello, *Chem. Rev.*, 2012, **112**, 2739–2779.
33 Y. Li, M. Zhou and R. Jin, *Adv. Mater.*, 2021, **33**, 2006591.
34 Z. Lin, N. Goswami, T. Xue, O. J. H. Chai, H. Xu, Y. Liu, Y. Su and J. Xie, *Adv. Funct. Mater.*, 2021, **31**, 2105662.
35 Y. Li, M. Zhou, Y. Song, T. Higaki, H. Wang and R. Jin, *Nature*, 2021, **594**, 380–384.
36 X.-M. Luo, C.-H. Gong, F. Pan, Y. Si, J.-W. Yuan, M. Asad, X.-Y. Dong, S.-Q. Zang and T. C. Mak, *Nat. Commun.*, 2022, **13**, 1177.
37 W. D. Liu, J. Q. Wang, S. F. Yuan, X. Chen and Q. M. Wang, *Angew. Chem.*, 2021, **60**, 11430–11435.
38 Q. Yao, T. Chen, X. Yuan and J. Xie, *Acc. Chem. Res.*, 2018, **51**, 1338–1348.
39 K. Sridharan, *The Electromagnetic Spectrum*, 2016, pp. 1–12.
40 A. Manchon and A. Belabbes, *Solid State Phys.*, 2017, **68**, 1–89.
41 S. Drummer, T. Madzimbamuto and M. Chowdhury, *Materials*, 2021, **14**, 2700.
42 D. A. Panayotov, A. I. Frenkel and J. R. Morris, *ACS Energy Lett.*, 2017, **2**, 1223–1231.
43 J. Zheng, P. R. Nicovich and R. M. Dickson, *Annu. Rev. Phys. Chem.*, 2007, 409–431.

44 R. Jin, Y. Zhu and H. Qian, *Chem.–Eur. J.*, 2011, **17**, 6584–6593.
45 C. Zhou, C. Sun, M. Yu, Y. Qin, J. Wang, M. Kim and J. Zheng, *J. Phys. Chem. C*, 2010, **114**, 7727–7732.
46 X. Qu, Y. Li, L. Li, Y. Wang, J. Liang and J. Liang, *J. Nanomater.*, 2015, **2015**, 1–23.
47 L. Zhang and E. Wang, *Nano Today*, 2014, **9**, 132–157.
48 A. Mathew and T. Pradeep, *Part. Part. Syst. Charact.*, 2014, **31**, 1017–1053.
49 Y. C. Shiang, C. C. Huang, W. Y. Chen, P. C. Chen and H. T. Chang, *J. Mater. Chem.*, 2012, **22**, 12972–12982.
50 W. Jahn and J. Stru, *Biol.*, 1999, **127**, 106–112.
51 R. Jin, *Nanoscale*, 2010, **2**, 343–362.
52 Y. An, Y. Ren, M. Bick, A. Dudek, E. H.-W. Waworuntu, J. Tang, J. Chen and B. S. Chang, *Biosens. Bioelectron.*, 2020, **154**, 112078.
53 X. Hu, T. Liu, Y. Zhuang, W. Wang, Y. Li, W. Fan and Y. Huang, *TrAC, Trends Anal. Chem.*, 2016, **77**, 66–75.
54 Z. Wang, B. Chen and A. L. Rogach, *Nanoscale Horiz.*, 2017, **2**, 135–146.
55 T. Qing, K. Zhang, Z. Qing, X. Wang, C. Long, P. Zhang, H. Hu and B. Feng, *Microchim. Acta*, 2019, **186**, 670.
56 Z. Yuan, Y.-C. Chen, H.-W. Li and H.-T. Chang, *Chem. Commun.*, 2014, **50**, 9800–9815.
57 M. Zhang, Y.-Q. Liu, C.-Y. Yu, B.-C. Yin and B.-C. Ye, *Analyst*, 2013, **138**, 4812–4817.
58 E. Thyrhaug, S. A. Bogh, M. R. Carro-Temboury, C. S. Madsen, T. Vosch and D. Zigmantas, *Nat. Commun.*, 2017, **8**, 15577.
59 J. M. J. Santillan, D. M. Arboleda, D. Muraca, D. C. Schinca and L. B. Scaffardi, *Sci. Rep.*, 2020, **10**, 8217.
60 G. Booth, Dyes, General Survey, *Ullmann's Encyclopedia of Industrial Chemistry*, Wiley-VCH, 2000, ISBN 3527306730, DOI: **10.1002/14356007.a09_073**.
61 B. Lellis, C. Z. Fávaro-Polonio, J. Alencar Pamphile and J. C. Polonio, *Biotechnol. Res. Int.*, 2019, **3**, 275–290.
62 M. Benjelloun, Y. Miyah, G. A. Evrendilek, F. Zerrouq and S. Lairini, *Arabian J. Chem.*, 2021, **4**, 103031.
63 S. B. Wang and H. T. LI, *Dyes Pigm.*, 2007, **72**, 308.
64 Y. Wang and J. YU, *Water Res.*, 1999, **33**, 3512.
65 A. K. Mittal and C. Venkobachar, *J. Environ. Eng.*, 1993, **119**, 366.
66 S. Mondal, *Environ. Eng. Sci.*, 2008, **25**, 1–10.
67 H. M. Solayman, M. A. Hossen, A. A. Aziz and N. Y. Yahya, *J. Environ. Chem. Eng.*, 2023, **11**, 109610.
68 X. Liu, W. Li, N. Chen, X. Xing, C. Dong and Y. Wang, *RSC Adv.*, 2015, **5**, 34456–34465.
69 Y. Liu, H. Yu, Z. Lv, S. Zhan, J. Yang, X. Peng, Y. Ren and X. Wu, *J. Environ. Sci.*, 2012, **24**, 1867–1875.
70 Z. Aksu, *Process Biochem.*, 2005, **40**, 997–1026.
71 B. Appavu, S. Thiripuranthagan, S. Ranganathan, E. Erusappan and K. Kannan, *Ecotoxicol. Environ. Saf.*, 2018, **151**, 118–126.
72 D. Pathania, S. Sharma and P. Singh, *Arabian J. Chem.*, 2017, **10**, S1445–S1451.
73 E. Haque, J. W. Jun and S. H. Jhung, *J. Hazard. Mater.*, 2011, **185**, 507–511.
74 W. Deligeer, Y. W. Gao and Y. Asuha, *Appl. Surf. Sci.*, 2011, **257**, 3524–3528.
75 V. Ponnusami, S. Vikram and S. N. Srivastava, *J. Hazard. Mater.*, 2008, **152**, 276–286.
76 T. Chen, Y. Zheng, J. Lin and G. Chen, *J. Am. Soc. Mass Spectrom.*, 2008, **19**, 997–1003.
77 P. C. Dey and R. Das, *Spectrochim. Acta, Part A*, 2020, 118122.
78 K. V. K. Rao, *Toxicol. Lett.*, 1995, **81**, 107–113.
79 Y. Chen, Y. Zhang, C. Liu, A. Lu and W. Zhang, *Int. J. Photoenergy*, 2011, **2012**, 1–6.
80 S. D. Richardson, C. S. Wilson and K. A. Rusch, *Ground Water*, 2004, **42**, 678.
81 R. Nagaraja, N. Kottam, C. R. Girija and B. M. Nagabhushana, *Powder Technol.*, 2012, **91**, 215–216.
82 M. S. Samuel, K. V. Savunthari and S. Ethiraj, *Environ. Sci. Pollut. Res.*, 2021, **28**, 40835–40843.
83 K. Iqbal, A. Iqbal, A. M. Kirillov, W. Liu and Y. Tang, *Inorg. Chem.*, 2018, **57**, 13270–13278.
84 K. Iqbal, A. Iqbal, A. M. Kirillov, C. Shan, W. Liu and Y. Tang, *J. Mater. Chem. A*, 2018, **6**, 4515–4524.
85 X. Luo, R. Abazari, M. Tahir, W. K. Fan, A. Kumar, T. Kalhorizadeh, A. M. Kirillov, A. R. Amani-Ghadim, J. Chen and Y. Zhou, *Coord. Chem. Rev.*, 2022, **461**, 214505.
86 X. H. Li, Y. Liu, H. Y. Lin, N. Xu, Z. Zhang, G. C. Liu and X. L. Wang, *Cryst. Growth Des.*, 2022, **22**, 3845–3852.
87 C. Xie, X. Wen, C. Xiao and S. Wei, *Water, Air, Soil Pollut.*, 2020, **231**, 280.
88 J. D. Vassallo, *Toxicol. Sci.*, 2004, **80**, 249–257.
89 S. L. Born, *Food Chem. Toxicol.*, 2003, **41**, 247–258.
90 S. A. Abouelmagd, F. Meng, B.-K. Kim, H. Hyun and Y. Yeo, *ACS Biomater. Sci. Eng.*, 2016, **2**, 2294–2303.
91 H. Qian, M. Zhu, Z. Wu and R. Jin, *Acc. Chem. Res.*, 2012, **45**, 1470–1479.
92 P. Maity, S. Xie, M. Yamauchi and T. Tsukuda, *Nanoscale*, 2012, **4**, 4027–4037.
93 R. Jin, *Nanoscale*, 2010, **2**, 343–362.
94 I. Russier-Antoine, F. Bertorelle, M. Vojkovic, D. Rayane, E. Salmon, C. Jonin, P. Dugourd, R. Antoine and P.-F. Breveta, *Nanoscale*, 2014, **6**, 13572–13578.
95 R. Philip, P. Chantharasupawong, H. Qian, R. Jin and J. Thomas, *Nano Lett.*, 2012, **12**, 4661–4667.
96 G. Ramakrishna, O. Varnavski, J. Kim, D. Lee and T. Goodson, *J. Am. Chem. Soc.*, 2008, **130**, 5032–5033.
97 M. S. Devadas, S. Bairu, H. Qian, E. Sinn, R. Jin and G. Ramakrishna, *J. Phys. Chem. Lett.*, 2011, **2**, 2752–2758.
98 P. Apell, R. Monreal and S. Lundqvist, *Phys. Scr.*, 1988, **38**, 174–179.
99 D. Lee, R. L. Donkers, G. L. Wang, A. S. Harper and R. W. Murray, *J. Am. Chem. Soc.*, 2004, **126**, 6193–6199.
100 O. J. H. Chai, Z. Liu, T. Chen and J. Xie, *Nanoscale*, 2019, **11**, 20437–20448.
101 A. Wang, X. Y. Liu, C.-Y. Mou and T. Zhang, *J. Catal.*, 2013, **308**, 258–271.
102 M. Ganguly, J. Jana, A. Pal and T. Pal, *RSC Adv.*, 2015, **6**, 17683–17703.
103 M. Ganguly, C. Mondal, J. Pal, A. Pal, Y. Negishi and T. Pal, *Dalton Trans.*, 2014, **43**, 11557–11565.

104 T. Y. Zhou, L. P. Lin, M. C. Rong, Y. Q. Jiang and X. Chen, *Anal. Chem.*, 2013, **85**, 9839–9844.
105 S. Kumar, M. D. Bolan and T. P. Bigioni, *J. Am. Chem. Soc.*, 2010, **132**, 13141–13143.
106 T. U. B. Rao and T. Pradeep, *Angew. Chem.*, 2010, **49**, 4218.
107 C. I. Richards, S. Choi, J. C. Hsiang, Y. Antoku, T. Vosch, A. Bongiorno, Y. L. Tzeng and R. M. Dickson, *J. Am. Chem. Soc.*, 2008, **130**, 5038–5039.
108 J. Sharma, H. C. Yeh, H. Yoo, J. H. Werner and J. S. Martinez, *Chem. Commun.*, 2010, **46**, 3280–3282.
109 S. Aslanzadeh, *J. Mol. Model.*, 2016, **7**, 160.
110 K. Naseem, Z. H. Farooqi, R. Begum, W. Wu, A. Irfan and A. G. Al-Sehemi, *Macromol. Chem. Phys.*, 2018, **219**, 1800211.
111 K. H. H. Aziz, *et al.*, *J. Hazard. Mater.*, 2018, **343**, 107.
112 M. Anari-Anaraki and A. Nezamzadeh-Ejhieh, *J. Colloid Interface Sci.*, 2015, **440**, 272.
113 M. Borandegi and A. Nezamzadeh-Ejhieh, *Colloids Surf., A*, 2015, **479**, 35.
114 A. Nezamzadeh-Ejhieh and M. Kabiri-Samani, *J. Hazard. Mater.*, 2013, **260**, 339.
115 A. Nezamzadeh-Ejhieh and M. Karimi-Shamsabadi, *Chem. Eng. J.*, 2013, **228**, 631.
116 H. Shirzadi and A. Nezamzadeh-Ejhieh, *J. Mol. Liq.*, 2017, **230**, 221.
117 A. Hernandez-Martínez, *React. Funct. Polym.*, 2018, **122**, 75.
118 F. Salimi, S. S. Emami and C. Karami, *Inorg. Nano-Met. Chem.*, 2018, **48**, 31.
119 F. Salimia, M. Eskandaria and C. Karamib, *Desalin. Water Treat.*, 2017, **85**, 206.
120 F. Salimi, K. Tahmasobi, C. Karami and A. Jahangiri, *J. Mex. Chem. Soc.*, 2017, **61**, 250.
121 H. Derikvandi and A. Nezamzadeh-Ejhieh, *J. Colloid Interface Sci.*, 2017, **490**, 628.
122 Y. Yu, C. Zhao, X. Liu, M. Sui and Y. Meng, *J. Environ. Chem. Eng.*, 2017, **5**, 5406.
123 M. Nasrollahzadeh, Z. Issaabadi and S. M. Sajadi, *RSC Adv.*, 2018, **8**, 3723.
124 M. Nasrollahzadeh, M. Sajjadi and S. M. Sajadi, *Chin. J. Catal.*, 2018, **39**, 109.
125 H. Zhang, G. Xue, H. Chen and X. Li, *Chemosphere*, 2018, **191**, 64.
126 Y. Li, S. Guo, H. Yang, Y. Chao, S. Jiang and C. J. R. Wang, *RSC Adv.*, 2018, **8**, 8057.
127 N. Demirkıran, G. T. Özdemir, M. Saraç and M. Dardagan, *Mong. J. Chem.*, 2017, **18**, 5.
128 J. Najeeb, G. Ahmad, S. Nazir, K. Naseem and A. Kanwal, *Korean J. Chem. Eng.*, 2017, 1.
129 M. Ikram, *RSC Adv.*, 2020, **10**, 20559.
130 A. Raza, *Appl. Nanosci.*, 2020, **10**, 3875.
131 A. N. Ejhieh and M. Khorsandi, *J. Hazard. Mater.*, 2010, **176**, 629.
132 M. Bahrami and A. Nezamzadeh-Ejhieh, *Mater. Sci. Semicond. Process.*, 2015, **30**, 275.
133 A. Raza, *Appl. Nanosci.*, 2020, **10**, 1535.
134 M. Ikram, A. Raza, M. Imran, A. Ul-Hamid, A. Shahbaz and S. Ali, *Nanosci. Res. Lett.*, 2020, **15**, 95.
135 M. Ikram, M. I. Khan, A. Raza, M. Imran, A. Ul-Hamid and S. Ali, *Phys. E*, 2020, **124**, 114246.
136 T. Shahwan, *Chem. Eng. J.*, 2011, **172**, 258.
137 B. Neppolian, H. Choi, S. Sakthivel, B. Arabindoo and V. Murugesan, *J. Hazard. Mater.*, 2002, **89**, 303.
138 Z. Shams-Ghahfarokhi and A. Nezamzadeh-Ejhieh, *Mater. Sci. Semicond. Process.*, 2015, **39**, 265.
139 C. Guillard, H. Lachheb, A. Houas, M. Ksibi, E. Elaloui and J.-M. Herrmann, *J. Photochem. Photobiol., A*, 2003, **158**, 27.
140 M. Ikram, *RSC Adv.*, 2020, **10**, 30007.
141 M. Ikram, *RSC Adv.*, 2020, **10**, 24215.
142 Z. Luo, X. Yuan, Y. Yu, Q. Zhang, D. T. Leong, J. Y. Lee and J. Xie, *J. Am. Chem. Soc.*, 2012, **134**, 16662.
143 J. Zhang, L. Qu, G. Shi, J. Liu, J. Chen and L. Dai, *Angew. Chem.*, 2016, **55**, 2230.
144 W. Kurashige, R. Kumazawa, D. Ishii, R. Hayashi, Y. Niihori, S. Hossain, L. V. Nair, T. Takayama, A. Iwase, S. Yamazoe, T. Tsukuda, A. Kudo and Y. Negishi, *J. Phys. Chem. C*, 2018, **122**, 13669.
145 R. Ullah and J. Dutta, *J. Hazard. Mater.*, 2008, **156**, 194.
146 S. Chandra, G. Beaune, N. Shirahata and F. M. Winnik, *J. Mater. Chem. B*, 2017, **5**, 1363.
147 S. Chandra, Nonappa, G. Beaune, A. Som, S. Zhou, J. Lahtinen, H. Jiang, J. V. I. Timonen, O. Ikkala and R. H. A. Ras, *Adv. Opt. Mater.*, 2019, **7**, 1900620.
148 N. Vilar-Vidal, J. Rivas and M. A. López-Quintela, *ACS Catal.*, 2012, **2**, 1693–1697.
149 C. Yu, G. Li, S. Kumar, H. Kawasaki and R. Jin, *J. Phys. Chem. Lett.*, 2013, **4**, 2847–2852.
150 S. Zhou, Y. Duan, F. Wang and C. Wang, *Nanoscale*, 2017, **9**, 4981–4988.
151 S. Bhattacharyya, B. Jana and A. Patra, *ChemPhysChem*, 2015, **16**, 796–804.
152 M. K. Barma, B. Paramanik, D. Bain and A. Patra, *Chemistry*, 2016, **22**, 11699–11705.
153 X. Yang, A. Wolcott, G. Wang, A. Sobo, R. C. Fitzmorris, F. Qian, J. Z. Zhang and Y. Li, *Nano Lett.*, 2009, **9**, 2331–2336.
154 Y. Hou, Z. Wen, S. Cui, X. Feng and J. Chen, *Nano Lett.*, 2016, **16**, 2268–2277.
155 Q. Zhang, Y. Huang, L. Xu, J. Cao, W. Ho and S. C. Lee, *ACS Appl. Mater. Interfaces*, 2016, **8**, 4165–4174.
156 B. Wu, Y. Xiong and Y. Ge, *Chem. Eng. J.*, 2018, **331**, 343–354.
157 U. Bali and B. Karagözoğlu, *Dyes Pigm.*, 2007, **74**, 73–80.
158 M. Cheng, G. M. Zeng, D. L. Huang, C. Lai, Y. Liu, C. Zhang, J. Wan, L. Hu, C. Y. Zhou and W. P. Xiong, *Water Res.*, 2018, **138**, 7–18.
159 H. Zhang, L. H. Guo, D. Wang, L. Zhao and B. Wan, *ACS Appl. Mater. Interfaces*, 2015, **7**, 1816–1823.
160 A. Khan, U. Alam, D. Ali, D. Bahnemann and M. Muneer, *Mater. Lett.*, 2018, **220**, 50–53.
161 M. Najafi, A. Abbasi, M. Masteri-Farahani and J. Janczak, *Dalton Trans.*, 2015, **44**, 6089–6097.
162 Q. Liu, D. Li, X. Lei, Y. Chen, J. Wang, A. Liu, B. Han and G. He, *Sep. Purif. Technol.*, 2023, **310**, 122938.
163 Y. Wang, Y. Tan, Y. Ding, L. Fu and W. Qing, *Colloids Surf., A*, 2022, **654**, 130072.

164 H. Zhang, L. H. Guo, D. Wang, L. Zhao and B. Wan, *ACS Appl. Mater. Interfaces*, 2015, **7**, 1816–1823.
165 T. Goswami, A. Bheemaraju, A. K. Sharma and S. Bhandari, *Colloid Polym. Sci.*, 2021, **299**, 925–936.
166 Y. Liu, Q. Yao, X. Wu, T. Chen, Y. Ma, C. N. Ong and J. Xie, *Nanoscale*, 2016, **8**, 10145–10151.
167 T. Goswami, M. Singh and K. M. Reddy, *Mater. Res. Bull.*, 2018, **107**, 286–294.
168 N. K. Chaki, J. Sharma, A. B. Mandle, I. S. Mulla, R. Pasricha and K. Vijayamohanan, *Phys. Chem. Chem. Phys.*, 2004, 1304–1309.
169 A. Bheemaraju, T. Goswami and M. Reddy, *ChemistrySelect*, 2019, **4**, 6790–6799.
170 N. K. Pal and C. Kryschi, *J. Mol. Catal. A: Chem.*, 2015, 404.
171 M. S. Bootharaju and T. Pradeep, *Langmuir*, 2013, **29**, 8125–8132.
172 C. Yu, G. Li, S. Kumar, H. Kawasaki and R. Jin, *J. Phys. Chem. Lett.*, 2013, **4**, 2847–2852.
173 K. Sridharan, E. Jang, J. H. Park, J.-H. Kim, J.-H. Lee and T. J. Park, *Chem. –Eur. J.*, 2015, **21**, 9126–9132.
174 L. Collado, A. Reynal, F. Fresno, M. Barawi, C. Escudero, V. Perez-Dieste, J. M. Coronado, D. P. Serrano, J. R. Durrant and V. A. de la Pena O'Shea, *Nat. Commun.*, 2018, **9**, 1–10.
175 S. Nair and B. J. Tatarchuk, *Fuel*, 2010, **89**, 3218–3225.
176 A. Arenas-Vivo, S. Rojas, I. Ocana, A. Torres, M. Liras, F. Salles, D. Arenas- Esteban, S. Bals, D. Avila and P. Horcajada, *J. Mater. Chem. A*, 2021, **9**, 15704–15713.
177 M. Farrang, *J. Photochem. Photobiol., A*, 2021, **422**, 113551.
178 C. Liu, X.-Q. Ren, F. Lin, X.-M. Fu, X.-Z. Lin, T. Li, K.-J. Sun and J.-H. Huang, *Angew. Chem., Int. Ed.*, 2019, **58**, 11335.
179 C. Deng, C. Sun, Z. Wang, Y. Tao, Y. Chen, J. Lin, G. Luo, B. Lin, D. Sun and L. Zheng, *Angew. Chem.*, 2020, **59**, 12659–12663.
180 T. Goswami, M. Reddy, A. K. Mishra and M. Singh, *ChemistrySelect*, 2018, **3**, 10892–10899.
181 N. Balázs, K. Mogyorósi, D. F. Srankó, A. Pallagi, T. Alapi, A. Oszkó, A. Dombi and P. Sipos, *Appl. Catal., B*, 2008, **84**, 356–362.
182 P. V. Kamat, *Chem. Rev.*, 1993, **93**, 267–300.
183 D. Mott, N. T. Thuy, Y. Aoki and S. Maenosono, *Philos. Trans. R. Soc., A*, 2010, **368**, 4275–4292.
184 K. P. Charle, L. Konig, S. Nepijko, I. Rabin and W. Schulze, *Cryst. Res. Technol.*, 1998, **33**, 1085–1096.
185 T. M. O. Le, T. H. Lam, T. N. Pham, T. C. Ngo, N. D. Lai, D. B. Do and V. M. Nguyen, *Polymers*, 2018, **10**, 633.
186 S. Mao, S. Ning, X. Zhang, M. Xia and F. Wang, *Adv. Powder Technol.*, 2021, **5**, 1641–1652.
187 R. Nagaraja, N. Kottam, C. R. Girija and B. M. Nagabhushana, *Powder Technol.*, 2012, **215**, 91–97.
188 A. Kumar and G. Pandey, *Mater. Sci. Eng. Int. J.*, 2017, **1**, 00018.
189 K. Negi, A. Umar, M. S. Chauhan and M. S. Akhtar, *Ceram. Int.*, 2019, **45**, 20509–20517.
190 M. Koklioti, I. Saucedo- Orozco, M. Quintana and N. Tagmatarchis, *Mater. Res. Bull.*, 2019, 114.
191 A. V. Salker and S. D. Gokakakar, *Int. J. Phys. Sci.*, 2005, **4**, 377–384.
192 V. P. Dinesh, P. Bijli, A. Ashok, S. K. Dhara, M. Kamruddin, A. K. Tyagi and B. Raj, *RSC Adv.*, 2014, **4**, 58930–58940.
193 J. Gonzalez-Rodriguez, L. Fernandez, Y. B. Bava, D. Buceta, C. Vazquez, M. A. Lopez-Quintela, G. Feijoo and M. T. Moreira, *Catalysts*, 2020, **10**, 31.
194 M. Reddy and J. Devaraju, *Mater. Today: Proc.*, 2019, **17**, 235–238.
195 M. Jakob, H. Levanon and P. V. Kamat, *Nano Lett.*, 2003, **3**, 353.
196 Z. Yuanhui, Z. Lirong, Z. Yingying, L. Xingyi, L. Z. Qi and W. Kemei, *Inorg. Chem.*, 2007, **46**, 6980–7986.
197 R. Agrawal and L. Mulky, *ChemBioEng*, 2023, **10**, 326–335.
198 M. S. Bootharaju and T. Pradeep, *Langmuir*, 2013, **29**, 812532.
199 W. Baschong, J. M. Lucocq and J. Roth, *Histochemistry*, 1985, **83**, 409.
200 N. Chandrasekharan, P. V. Kamat, J. Hu and G. Jones, *J. Phys. Chem. B*, 2000, **47**, 11103–11109.
201 M. R. Willner and P. J. Vikesland, *J. Nanobiotechnol.*, 2018, **16**, 1–16.
202 K. E. Sapsford, L. Berti and I. L. Medintz, *Angew. Chem.*, 2006, **45**, 4562–4588.
203 U. Resch-Genger, M. Grabolle, S. Cavaliere-Jaricot, R. Nitschke and T. Nann, Quantum dots versus organic dyes as fluorescent labels, *Nat. Methods*, 2008, **5**, 763–775.
204 R. D. Mitra, C. M. Silva and D. C. Youvan, *Gene*, 1996, **173**, 13–17.
205 I. L. Medintz, A. R. Clapp, H. Mattoussi, E. R. Goldman, B. Fisher and J. M. Mauro, *Nat. Mater.*, 2003, **2**, 630–638.
206 N. Y. chen, H. F. Li, Z. F. Gao and F. Qu, *Sens. Actuators, B*, 2014, **193**, 730–736.
207 B. E. Demirhah, H. E. S. Kara and B. Dehmirahan, *J. Photochem. Photobiol., A*, 2021, **417**, 113356.